Luminescence of iron ions in crystals: Site occupancy, valence states, and excited-state properties

Qiaoling Chen [1,2,*] Chang Ji,[1,2] and Chang-Kui Duan [1,2,3,†]

[1]*CAS Key Laboratory of Microscale Magnetic Resonance and Department of Physics, School of Physical Sciences,*
University of Science and Technology of China, Hefei 230026, China
[2]*CAS Center for Excellence in Quantum Information and Quantum Physics,*
University of Science and Technology of China, Hefei 230026, China
[3]*Hefei National Laboratory, University of Science and Technology of China, Hefei 230088, China*

Iron ions play significant roles as recombination centers and activators in insulators. However, their identification and mechanisms through which they operate are often controversial. In this study, we utilized first-principles calculations to investigate the site occupancy, valence states, excited states, and optical properties of iron ions acting as luminescent centers. We also explored potential quenching processes when these ions serve as recombination centers in various crystals. We found that iron ions can occupy sites with tetrahedral, octahedral and dodecahedral coordinations. Specifically, tetrahedrally coordinated Fe^{3+} in oxide insulators exhibit near-infrared emission in the range of 670–830 nm, with the specific wavelength dependent on the degree of structure distortion. In contrast, octahedrally coordinated Fe^{3+} ions in spinels and garnets exhibit considerably lower transition energies due to stronger ligand fields and significant excited-state structural relaxation. This makes them more susceptible to nonradiative decay and quenching. We also successfully elucidated the luminescence of those six-coordinated Fe^{3+} in perovskites, where the weaker ligand fields and smaller excited-state relaxation than those in spinels and garnets contribute to the observed emissions. Furthermore, we have confirmed the existence of dodecahedrally coordinated Fe^{3+} in hosts with a zircon structure, which results in a large transition energy due to the combined effect of the small nephelauxetic effect in phosphates and the small ligand field strengths associated with a subspherical coordination distribution. Additionally, we revisited and reinterpreted some experimental results based on our calculations. This study offers consistent and reliable interpretations of optical transitions of iron impurities in solids, which can be beneficial for the design and optimization of luminescent materials.

I. INTRODUCTION

Unintentional incorporated transition metal impurities in insulators usually result in deep defect states in the band gaps, leading to radiative or nonradiative recombination processes in luminescent materials. Due to its high abundance in many source materials, iron is a common contaminant. The recombination effects of iron contamination have been extensively studied in scintillators, as well as III-V and II-VI compound semiconductors [1–3]. For instance, the laser performance of $In_xGa_{1-x}As$ is often limited by iron impurity, which acts as an effective deactivation [4]. Iron impurities also serve as an efficient quenching center for visible photoluminescence in ZnS *via* strong photoionization ($Fe^{2+} \rightarrow Fe^{3+}$) process [5]. Also in ZnS, emissions at 0.98 and 1.25 µm were attributed to $^3T_1 \rightarrow {}^5E$ transition of Fe^{2+} impurity [6] and $^4T_1 \rightarrow {}^6A_1$ transition of Fe^{3+} impurity [2], respectively. The 1.45 µm emission was originally attributed to $^3T_1 \rightarrow {}^5T_2$ transition of Fe^{2+} impurity [5], but was latter attributed to $^2E \rightarrow {}^2T_2$ transition of Cu^{2+} impurity [2]. Luminescence due to iron contamination has led to complications and confusions in

luminescent center identification. For instance, a near-infrared afterglow phosphor reported in Mg_2SnO_4 crystal was originally attributed to the intrinsic defects [7], but was latter realized as unintentional incorporated iron and manganese impurities [8]. The photoluminescence previously misidentified as from Bi^{3+} activators in $MAl_{12}O_{19}$ was clarified by a combination of theoretical and experimental study as from iron impurity activators [9].

Recently, near-infrared (NIR) phosphors have gained significant attention due to their immense potential in plant growth, night vision monitoring, biomedical imaging, and so forth. Various transition metal ions, Cr^{3+}, Cr^{4+}, Ni^{2+}, Fe^{3+}, post-transition metal Bi^+, Bi^0, and rare-earth ions, Nd^{3+}, Ho^{3+}, Er^{3+}, Tm^{3+}, Yb^{3+} [10], and even Eu^{2+} [11] have been introduced into inorganic host materials to produce NIR luminescence. Among these ions, iron is not only abundant in nature but also environmentally benign and biologically compatible. The development of Fe^{3+}-based NIR-emitting phosphors has been substantial [12]. However, the identification and understanding of the luminescence mechanisms of iron-related phosphors remain an unresolved issue. For instance, in the inverse spinel $LiAl_5O_8$ or $LiGa_5O_8$ crystal host, a dominant luminescence peaking at 665 and 680 nm was assigned to the tetrahedrally coordinated Fe^{3+}, while a weak emission peaking at 725 and 740 nm was assigned

*cql@ustc.edu.cn
†ckduan@ustc.edu.cn

to the octahedrally coordinated Fe^{3+} [13]. Later, a sharp zero-phonon line at 1115 nm with the phonon sideband extending to around 1400 nm was reported in $LiGa_5O_8$ host, which was attributed to the luminescence of the octahedral coordinated Fe^{3+} activators [14]; while in α-Ga_2O_3 host an emission peaking at 950 nm was reported [15], which was also assigned as the octahedral coordinated Fe^{3+} activators. The diversified emissions attributed to octahedral sites appear to be contradictory, given the expected similarity in the crystal environments of Fe^{3+} in these hosts. In recent years, Fe^{3+}-doped NIR-emitting phosphors have been developed. However, achieving efficient NIR emission still continues to be challenging. Fe^{3+}-doped $KAl_{11}O_{17}$ serves as a representative example. It produces a broad NIR emission band peaking at about 770 nm and exhibiting no apparent thermal quenching up to 200 °C [16]. The site occupancy of iron activators was discussed, and temperature and concentration dependent emission spectra were measured to verify the energy transfer and weak electron-phonon coupling. Double-perovskite compounds, which typically have octahedral sites, have been studied for Fe^{3+} activators, and a high internal quantum efficiency of 87% was achieved for Ca_2InSbO_6 : Fe^{3+} [17]. It is natural to compare the Fe^{3+} activator with its iso-electronic Mn^{2+}, which is also a significant activator, as both have the half filled $3d^5$ electronic configuration. Generally, the hybridization between d orbitals and ligand orbitals is larger for Fe^{3+} than for Mn^{2+} in solids as a result of closer orbital energies in Fe^{3+}. This leads to a stronger nephelauxetic effects [18] and larger ratios of the ligand-field strength relative to the effective Coulomb interaction for Fe^{3+} over Mn^{2+} in solids. Many Mn^{2+}-activated compounds have been found to produce green- or red-light phosphors, with the emission wavelengths being dominated by the coordination numbers. Fe^{3+} is expected to produce redshifted emission band relative to that of Mn^{2+} in similar surroundings.

Despite the rich phenomena of iron ions in solids as recombination centers and activators, our understanding of their site-occupancy, valence states, and excited-state properties such as optical transition mechanisms and energies, radiative and nonradiative relaxation remains incomplete. This highlights an urgent need for a systematically theoretical study to investigate the defect levels and optical transitions of iron in solids. Previous studies have primarily investigated the behavior of iron impurities in III-V and II-VI semiconductors [19–21]. First-principles calculations have proven effective in analyzing the defect levels of Fe-dopants and how they influence nonradiative recombination in nitrides [1]. The optical spectra of iron ions in some crystals have been analyzed based on the phenomenological crystal-field theory [3], the orbital energy differences, and excited-states calculations [22]. However, most works have focused on ground-state properties and relied on conventional semilocal functionals such as the local density approximation (LDA) or the generalized gradient approximation (GGA) [22–24]. Due to the delocalization shortcoming of LDA and GGA, GGA+U and hybrid functional calculations have become a natural choice in improving the descriptions of localization for the defect levels and optical transitions of transition metal ions in solids. Hybrid functional calculations for Fe in GaN demonstrated excellent agreement between calculated acceptor levels [25] and experimentally

measured absorption [3] and deep-level transient spectroscopy [26].

In this study, we utilized first-principles calculations grounded in density functional theory (DFT) to explore the excited states and optical transitions, and elucidate the luminescent mechanisms of iron dopants as recombination centers and activators. We investigated iron ions doped in a large variety of crystals, including the series of spinels (both normal and inverse), zircon structure crystals, garnets, perovskites, III-V and II-VI semiconductors, halides, and so forth. We included typical crystal hosts and typical site occupancies for Fe^{3+}, with photoluminescence covering a broad wavelength range from approximately 670 nm to over 1000 nm. We studied a wide range of systems with diverse compositions, structures, and optical transition properties. Our work has provided a detailed understanding of the luminescence mechanisms of iron activators in solids and has demonstrated the effectiveness of first-principles calculations as a theoretical tool for studying a wide range of iron-containing systems.

II. METHODOLOGY

A. Parameter settings

All calculations were performed using the Vienna *ab initio* simulation package (VASP) based on the density functional theory (DFT) [27,28]. The Perdew-Burke-Ernzerhof (PBE) functional [29] was adopted to describe exchange correlation functional, and the recommended projector augmented wave (PAW) method [30] for DFT calculations was used to treat the interaction between ion core and electrons. The kinetic-energy cutoff for the plane-wave basis was set to 400 eV. The conjugate gradient method was used for the geometric optimizations until the Hellmann-Feynman forces on atoms were less than 0.01 eV/Å. The comparison of calculated and experimental lattice parameters [31–46] and the corresponding supercell constructions for defect calculations are discussed in detail in the Supplemental Material [47]. The defect formation energy calculations were performed by the GGA + U method with $U = 4$ eV, $J = 1$ eV, which is a typical value for $3d$ transition-metal impurities (Refs. [48–51]; see the Supplemental Material for details [47]). The optical transition energy calculations were based on the HSE06 functionals. As a compromise between accuracy and computational resources of hybrid functional HSE06 calculations, only one Γ-point was applied to sample the Brillouin zone for the defect calculations in supercells. The influence of different U values, k-point meshes, and HSE06 on optimized structures and transition energies were performed to confirm the reliability of our approach (see more details in Note 1 of the Supplemental Material [47]).

B. Defect formation energy and charge state transition energy

In thermodynamic equilibrium, the formation energy and the associated concentration of a defect X^q are given by [52]

$$E^f[X^q] = (E_{tot}[X^q] + E_{corr}) - E_{tot}[bulk]$$
$$- \sum_i n_i \mu_i + q E_F, \tag{1}$$

$$c[X^q] = N_{site} \omega \exp(-E^f[X^q]/k_B T). \tag{2}$$

$E_{\text{tot}}[\text{bulk}]$ and $E_{\text{tot}}[X^q]$ are the total energy of a perfect supercell and the supercell containing the defect X^q, respectively. E_{corr}, a small correction to the total energy of the charged defects, is ignored here as it does not insignificantly affect the formation energy. μ_i and E_F are the chemical potential of type i atom species and the electrons reservoirs, respectively. n_i indicates the change in the number of type i atom species for the supercell containing the defect X^q relative to the perfect supercell. The defect concentration c is related to the Gibbs energy of formation of the defect, often approximated with the defect formation energy for solid phases. N_{sites} and ω are the numbers of available atomic sites for doping and the effective degeneracy factor of the defect, respectively.

It is shown by Eq. (2) that the chemical potentials of related atom species and the electrons are important for analyzing the defect concentrations. In principle, the chemical potentials are restricted for the existence of target crystal host and the depleted competing compounds. Besides, the chemical potential of gas-phase species can be related to partial pressure (p) and temperature (T), and for oxygen species [53],

$$\mu_O = \frac{1}{2}E_{O_2} + \Delta\mu_O, \tag{3a}$$

$$\Delta\mu_O = \frac{1}{2}k_B T\left[\ln\left(\frac{pV_Q}{k_B T}\right) - \ln Z_{\text{rot}} - \ln Z_{\text{vib}}\right], \tag{3b}$$

where $V_Q = (h^2/2\pi m k_B T)^{3/2}$, Z_{rot}, and Z_{vib} are the oxygen molecular quantum volume, the rotational partition function, and the vibrational partition function, respectively. E_{O_2} is the total energy of the spin-triplet of an O_2 molecule, which has been corrected by adding 1.36 eV per O_2 due to the overbinding of O_2 in GGA calculation [48], and the air atmosphere with a partial pressure of $p = 0.2$ atm for O_2 is applied. A systematic sintering temperature 1600 K is used for discussions. Considering that the effective equilibrium temperature of the oxygen-related defect is much lower than the sintering temperature due to the annealing process after sintering the sample, about 2/3 of the sintering temperature $T = 1100$ K is applied and $\Delta\mu_O = -1.3$ eV is obtained by Eq. (3) [54].

Another crucial parameter is the chemical potential of electrons, i.e., the Fermi energy E_F, which is not independent but constrained by the charge neutrality condition specified as follows [52]

$$\sum_{X,q} qc(X^q) + n_h - n_e = 0, \tag{4a}$$

$$n_e - n_h = 2\left(\frac{m_e k_B T}{2\pi\hbar^2}\right)^{3/2}\exp\left[(E_F - \epsilon_{\text{CBM}})/k_B T\right]$$
$$- 2\left(\frac{m_h k_B T}{2\pi\hbar^2}\right)^{3/2}\exp\left[(\epsilon_{\text{VBM}} - E_F)/k_B T\right]. \tag{4b}$$

Here, ϵ_{CBM} and ϵ_{VBM} represent the energies of the conduction-band minimum (CBM) and valence-band maximum (VBM), respectively. Once the chemical conditions are defined by coexistence conditions of chemical reactions or compositions of ingredients, the value E_F^0 of the Fermi energy parameter E_F is determined. In practice, for insulators, $n_e - n_h$ is generally negligible due to the large difference between E_F^0 and ϵ_{CBM} or ϵ_{VBM}. Therefore, E_F^0 can be estimated by the intersection

of the E_F-dependent formation energies of the dominant positively and negatively charged defects.

C. Excited states and geometric optimization

In the DFT framework, certain multiplet excited states can be approximated with a combination of single determinants. These determinants can be obtained using methods such as spin-multiplicity control or constrained occupancy. For a transition metal ion with octahedral or tetrahedral coordination, the five $3d$ orbitals split into sets: two degenerate e orbitals and three degenerate t_2 orbitals. The ground multiplet state of Fe^{3+}, denoted as $^6A_1$, has an electronic configuration of $e^2 t_2^3$. This state can be obtained by setting the spin sextet. In T_d symmetry, the main components of the $^6A_1$, $^4T_1$, $^4T_2$, ^4E, and $^4A_1$ multiplets are $e^2(^3A_2)t_2^3(^4A_2)$, $e^3(^2E)t_2^2(^3T_1)$, $e^3(^2E)t_2^2(^3T_1)$, $e^2(^3A_2)t_2^3(^2E)/e^2(^1E)t_2^3(^4A_2)$, and $e^2(^3A_2)t_2^3(^4A_2)$, respectively. The excited states $^4A_1$ and ^4E have similar energies and are mainly influenced by the Coulomb repulsion interaction. These excited states $^4A_1$ and ^4E, can be determined by the spin flip within the $e^2 t_2^3$ electronic configuration. The calculated energies of related Slater's determinants are related to those of the excited states $^4T_1$ and $^4E / ^4A_1$ as follows [55]:

$$E(|\xi\eta\bar{\epsilon}\theta\epsilon\rangle) = E(^4T_1), \tag{5a}$$

$$E(|\theta\epsilon\bar{\xi}\eta\zeta\rangle) \approx \frac{1}{5}E(^6A_1) + \frac{4}{5}E(^4E/^4A_1). \tag{5b}$$

Herein, θ and ϵ are partners of T_d or O point-group representation e and correspond to d_{z^2} and $d_{x^2-y^2}$ orbitals; ξ, η, ζ represent t_2-type orbitals d_{yz}, d_{xz}, and d_{xy}; and the overbarred orbitals are orbitals with minor spin. The schematic nominal electronic occupancy, the projected density of states and partial charge density distributions of ground $^6A_1$ state, excited $^4T_1$ and $^4A_1 / ^4E$ states are discussed in Figs. S1 and S2 of the Supplemental Material [47]. As a result of the stronger mixing of ligand orbitals for Fe^{3+}, which is closer to the VBM compared with Mn^{2+} occupying similar sites, the effective Coulomb interaction in d^5 of Fe^{3+} is significantly reduced relative to that of the free ion. Meanwhile, due to the mixing, the effective ligand field becomes more important. This has led to an increase in both Dq/B and the $E(^4A_1) - E(^4T_1)$ (approximate $10Dq - C$) for Fe^{3+}, compared with those of Mn^{2+}. Please note that, in this context, Dq refers to one-tenth of the t_2-e splitting, and B, C are the Racah parameters [56]. The $^4T_1$ excited states can be calculated using the spin quartet setting with little spin contamination in the lower-spin excited states [55]. Besides, the $^4A_1 / ^4E$ excited states can be calculated by the occupation matrix control methodology [55,57] with spin quartet setting. The Racah parameter B can calculated with $E(^4A_1 - ^6A_1) = (10 + 5C/B)B$ and the approximate ratio $C/B = 4.73$ for the Fe^{3+} free ion [56]. The ligand field strength Δ or $10Dq$ can be obtained by calculating the energy difference between the average energy of the e orbitals and that of the t_2 orbitals. This calculation involves equal occupancy of the five $3d$ orbitals in spin-unpolarized GGA calculations following the method used for evaluating the ligand field strength of Mn^{2+} in solids [55]. The $Fe^{3+} \rightarrow Fe^{2+} + h_{\text{VBM}}$ charge-transfer transition energy is estimated by $E_{\text{CT}}^{\text{abs}}(Fe^{3+}) = [E_{Fe^{3+}}(Fe^{2+}) - \epsilon_{\text{VBM}} +$
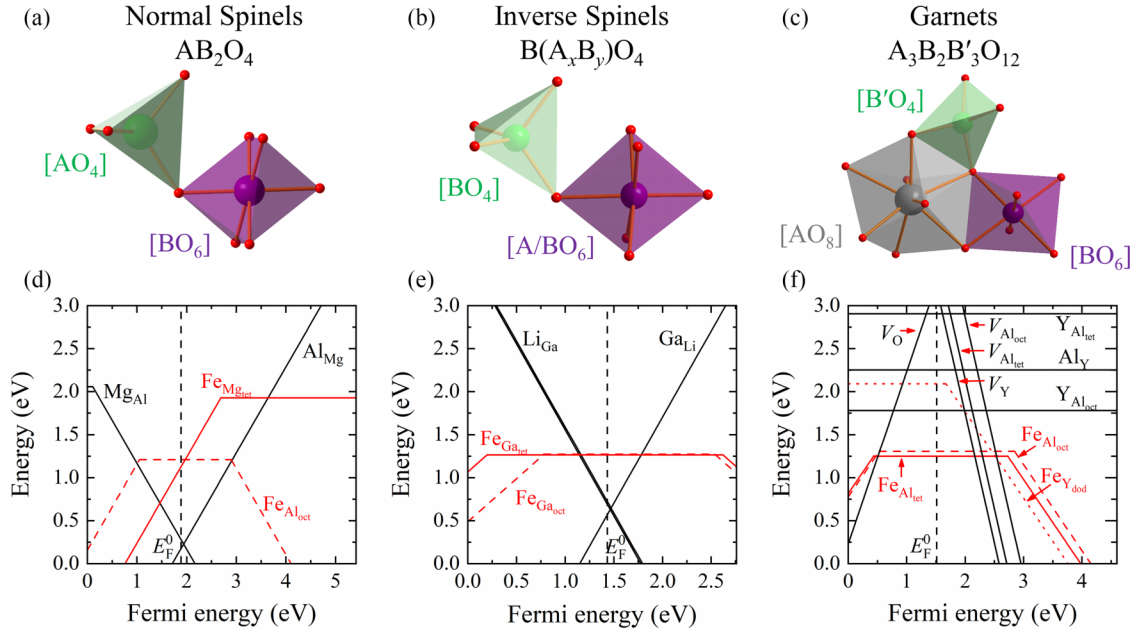
FIG. 1. (a)–(c) Local structures of octahedron, tetrahedron, or dodecahedron in AB_2O_4 normal spinels, $B(A_xB_y)O_4$ inverse spinels, and $A_3B_2B'_3O_{12}$ garnet crystals. (d)–(f) Formation energies vs Fermi energy of Fe dopants coordinated in octahedral (red dashed lines), tetrahedral (red solid lines), and dodecahedral (red dotted lines) structures, along with intrinsic defects (black solid lines) in $MgAl_2O_4$ normal spinel, $LiGa_5O_8$ inverse spinel and YAG garnet crystal hosts. Vertical dashed lines are E_F^0.

$E_{Coul}] - E_{Fe^{3+}}(Fe^{3+})$. The charge-transfer transition calculated with the dielectric-dependent hybrid functional ($\alpha \sim 0.9/\epsilon_\infty$) for wide band gap have shown an uncertainty about 0.2 eV. Here, two errors of opposite sign—overestimation by ignoring E_{Coul} and underestimation due to HSE06 functional for the band gap in insulators—are neglected [58].

The equilibrium structures of both the ground and excited states are obtained by geometric optimization with the corresponding Slater's determinants occupancy. In accordance with the Franck-Condon principle, the excitation and emission energies are obtained as the differences in total energy between the ground and excited states at the initial state's equilibrium geometric configurations for the corresponding transitions. The hybrid density functionals are employed for the calculations.

III. RESULTS AND DISCUSSIONS

A. Luminescence of Fe^{3+} in normal or inverse spinel crystals

Fe^{3+} activated normal or inverse spinels are common systems for visible or near-infrared phosphors and persistent luminescence materials [12,59,60]. There are many discussions available on the site occupancy and valence states of iron activators and other transition metal impurities in these spinel-type hosts, but controversies remain. These controversies hinder the understanding and improvement of iron-related materials. Here, we elucidate the multisite occupancy and multivalence states nature of iron ions, and determine the optical transition properties of Fe^{3+} in different coordinations to understand the luminescent mechanism and identify the luminescent centers.

A normal spinel crystal, formulated as AB_2O_4, comprises $[AO_4]$ tetrahedrons and $[BO_6]$ octahedrons, shown in

Fig. 1(a). In contrast, the inverse spinel $B(A_xB_y)O_4$ structure is in Fig. 1(b). Here, A and B ions in parentheses occupy octahedral coordinated sites, their proportions specified by x, y, while the other B ions occupy tetrahedral coordinated sites. For $LiAl_5O_8$, the tetrahedral site is occupied by Al, and octahedral coordinated sites are occupied by Li^+ and Al^{3+} ions with the ratio of 1:3. The structure of $LiGa_5O_8$ crystal is similar. For the Mg_2SnO_4 host, the octahedral site is occupied by Mg^{2+} and Sn^{4+} in the ratio of 1:1, and the tetrahedral site is occupied by Mg^{2+}. It is important to note that contributions from antisites have been taken into account in the above ratios. Here, we discuss the site occupancy and valence states of iron dopants in the prototype system of $MgAl_2O_4$ normal spinel and $LiGa_5O_8$ inverse spinel hosts. The excited states and optical transitions of Fe^{3+} are calculated and analyzed in all the spinel-type crystals.

In the normal spinel $MgAl_2O_4$ crystal, the formation energies of iron dopants and intrinsic defects are calculated, as shown in Fig. 1(d). Here, the equal formation enthalpy distribution of final compound to raw materials is used, i.e., $\Delta\mu_{MgO} = \Delta H_{MgAl_2O_4}^f/2$, and $\Delta\mu_{Al_2O_3} = \Delta H_{MgAl_2O_4}^f/2$. The chemical potential of oxygen, $\mu_O = 1/2E_{O_2} + \Delta\mu_O$, $\Delta\mu_O = -1.3$ eV is applied, and then $\mu_{Mg} = E_{MgO} + \Delta\mu_{MgO} - \mu_O$, $\mu_{Al} = (E_{Al_2O_3} + \Delta\mu_{Al_2O_3} - 3\mu_O)/2$. The chemical potential of iron μ_{Fe} is determined by a relative replacement concentration of 0.05% under the constraint that no precipitation of Fe-related compounds occurs. In this case, the defect concentrations of antisites dominate over others, and the Fermi energy E_F^0 is approximately determined by the intersection of the two antisite defects Mg_{Al}^- and Al_{Mg}^+. At this E_F^0, the defect formation energies of $Fe_{Mg_{tet}}^+$ (Fe_{tet}^{3+}) and $Fe_{Al_{oct}}^0$ (Fe_{oct}^{3+}) are comparable and both dominate over other valence states of iron. Thus, the iron impurity can occupy both tetrahedral

coordinated Mg^{2+} and octahedral coordinated Al^{3+} sites and mainly show Fe^{3+} valence state. Tuning the chemical-potential conditions have negligible influence on the site occupancy and valence states of iron. The negative formation energies at the upper limits of iron's possible chemical potentials demonstrate the ease of incorporating iron ions (see more details in Note 2 of the Supplemental Material [47]).

In the inverse spinel $LiGa_5O_8$ crystal, the formation energies of intrinsic defects and iron dopants are shown in Fig. 1(e). The equal formation enthalpy distribution of final compound to binary oxides is first considered, i.e., $\Delta\mu_{Li_2O} = \Delta H^f_{LiGa_5O_8}$, and $\Delta\mu_{Ga_2O_3} = \Delta H^f_{LiGa_5O_8}/5$. The chemical potentials μ_{Li}, μ_{Ga}, μ_O can be obtained with $\Delta\mu_{Li_2O}$, $\Delta\mu_{Ga_2O_3}$, and $\Delta\mu_O = -1.3$ eV. Then, the chemical potential of iron μ_{Fe} is determined by the doping concentration of 0.05%. In this case, the Li_{Ga} and Ga_{Li} antisite defects with oppositely divalent states are dominant. At this determined E^0_F, the defects formation energies of $Fe^0_{Ga_{tet}}$ (Fe^{3+}_{tet}) and $Fe^0_{Ga_{oct}}$ (Fe^{3+}_{oct}) are comparable. Iron impurity can occupy both tetrahedral and octahedral coordinated Ga^{3+} sites, and the tuning chemical potentials have negligible influence on the site occupancy and valence states of iron (see more details in Note 2 of the Supplemental Material [47]).

Formation energy results show the comparable concentration of tetrahedral and octahedral Fe^{3+}. Then, the excited states and optical properties of Fe^{3+} at both sites are discussed. As shown in Table I, the ligand field strength of octahedral Fe^{3+}_{oct}, Δ_{O_h}, is about 2.0 eV and much larger than that of tetrahedral Fe^{3+}_{tet}, $\Delta_{T_d} \approx 0.8$ eV. The average bond lengths of Fe^{3+}_{oct} with coordinations are slightly larger than that of Fe^{3+}_{tet} with coordinations, and Δ_{O_h} is about 9/4 times Δ_{T_d} by the static charge model. In the d^5 electronic configuration, Tanabe-Sugano theory [56] shows the decreasing $^4T_1$ excited states relative to that of $^6A_1$ ground state with the increasing Dq/B, which is consistent with our calculation results. As is shown, the $^4T_1 \leftrightarrow {}^6A_1$ transition energies of Fe^{3+}_{tet} are much larger than that of Fe^{3+}_{oct}.

Iron-doped spinels or inverse spinels have been extensively studied for near-infrared persistent luminescence due to the abundant vacancies and antisite defects [12]. In these spinel-type crystals, the ligand field strength of tetrahedrally coordinated Fe^{3+} is relatively small about 0.8–0.9 eV, and the emissions are in the range of 1.70–1.85 eV. The calculated emission energies of tetrahedral Fe^{3+} agree reasonable well with experiments, with the underestimation about 0.1 eV or less. The underestimation is at least partially due to spin contamination in excited states by mixing the ($S = 5/2$, $S_z = 3/2$) component of the ground multiplet state [55]. The underestimation due to spin contamination should be much less severe for octahedrally coordinated Fe^{3+} as a result of the much larger ligand field strength, which will be discussed in Sec. III C. Especially, iron-doped inverse spinels $LiAl_5O_8$ and $LiGa_5O_8$ have been extensively studied in earlier experiments and the luminescent identification of tetrahedral and octahedral Fe^{3+} is still unsolved. Fe^{3+}, Mn^{4+}, and Cr^{3+} activators in these hosts overlap in luminescent wavelength ranges [78], which often leads to complexities and ambiguities in identifying the luminescent centers. After thorough calculations and assessment of the experimental results, it can be concluded that in ordered $LiAl_5O_8$ crystal host, the luminescence with

zero-phonon line (ZPL) at about 658 nm and band maximum about 690 nm (1.80 eV) is due to the tetrahedral coordinated Fe^{3+} activators [64,67]. Fe^{3+} in disordered phase shows a redshifted emission with band maximum about 1.70 eV [68].

We now revisit the previously reported near-infrared emission peaking at around 1230 nm in iron-doped $LiGa_5O_8$, which was attributed to the octahedral coordinated Fe^{3+} [14]. However, our calculations predicted a vertical transition energy of merely 0.76 eV at the excited-state equilibrium geometric configuration, which is smaller than the observed emission peak by about 0.25 eV. Therefore, even considering the systematical calculation error of octahedral coordinated Fe^{3+} (see Sec. III C), this observed near-infrared emission is unlikely to be originated from Fe^{3+}_{oct}. Hence, we are considering other possibilities, such as those due to trace impurities. At low temperatures, the emission shows a sharp zero-phonon line at 1115 nm, while at room temperatures, the peak is about 1230 nm [14]. The emission's decay lifetime at 13 K is 1.12 ms [14]. In theory, Cr^{4+} can substitute a tetrahedral Al^{3+} or Ga^{3+} site with similar emission lineshape, but the luminescence decay time is much shorter, in the range of tens of microseconds [79]. Additionally, Ni^{2+} activators could replace the octahedral coordinated Al^{3+}, Ga^{3+}, or Li^+ ions in aluminogallate and zincalumino and lithiumalumino silicate glass ceramic systems. This substitution typically results in similar near-infrared emissions [80]. We noticed that the luminescence lineshape of Ni^{2+} in $LiGa_5O_8$ crystal [81] is similar to the measured luminescence lineshape reported in the iron-doped $LiGa_5O_8$ [14]. The lifetime of Ni^{2+} in $LiGa_5O_8$ crystal is approximately 500 μs at room temperature [80,82], which is compatible with that reported in iron-doped $LiGa_5O_8$ [14], considering difference in the temperature and thus the nonradiative rate. The luminescence of Ni^{2+} was redshifted from 1215 to about 1280 nm gradually when Sn^{4+} is incorporated in $LiGa_5O_8 : Ni^{2+}$ [83]. The emission peaking at about 1300 nm was reported in $LiGa_5O_8$ glass ceramics [82], and the similar luminescence may be attributed to the disorder crystal structure [84]. Formation energy calculations also support that the octahedral coordinated Ni^{2+} shows the lowest formation energy and highest defect concentration among the nickel-related defects (see more details in Note 2 of the Supplemental Material [47]). Therefore, we reassigned the near-infrared emission in $LiGa_5O_8$, previously attributed to Fe^{3+} activators, to Ni^{2+} impurity.

Luminescence similar to these from the tetrahedral site Fe^{3+} in $LiGa_5O_8$ has been reported in iron-doped β-$LiGaO_2$ [85,86]. β-$LiGaO_2$ contains only one inequivalent site for Ga^{3+} and one for Li^+, both with tetrahedral oxygen coordinations. Our calculations confirm that Fe^{3+} prefers occupying the Ga^{3+} site over the Li^+ site. The $^4T_1 \rightarrow {}^6A_1$ transition energy at the excited-state local minima of the tetrahedral Fe^{3+} is calculated to be 1.62 eV, aligning well with the experimentally observed emission peaking at 1.66 eV [85,86].

It has been shown that the emission energy of iron-doped $LiGaO_2$ decreases with the increase of pressure at a rate of -74 cm^{-1}/GPa in a broad range of pressures of 1.85–14.45 GPa. It is believed that the transition from phase β-$LiGaO_2$ to α-$LiGaO_2$ occurs at a pressure of 3 GPa or even lower. Our analysis above has indicated that Fe^{3+} at octahedral sites are unlikely to produce an emission at such energies.

TABLE I. Calculated charge-transfer excitation (Calc. CT), $^4T_1 \leftrightarrow {}^6A_1$ excitation and emission energies (Calc. exc., Calc. emi.), Stokes shifts (Calc. Stokes), ligand field strengths (Δ), experimentally observed emission (Expt. emi.) and onset and peak of CT excitation (Expt. OCT, PCT) of Fe^{3+} in a series of hosts (in units of eV). ZPL stands for zero-phonon line.

Host	Fe^{3+}	Δ	Calc. CT	Calc. exc.	Calc. emi.	Calc. Stokes	Expt. OCT (PCT)	Expt. emi.
Normal spinel								
$MgAl_2O_4$	$Fe^+_{Mg_{tet}}$	0.89	4.11 [a]	1.89	1.75	0.14	3.54 (4.43) [59]	1.73 [61]
	$Fe^0_{Al_{oct}}$	2.05		0.86	0.65	0.21		
$ZnAl_2O_4$	$Fe^+_{Zn_{tet}}$	0.90	3.77[a]	1.88	1.73	0.14	3.56 (4.28) [59]	1.76 [59]
$MgGa_2O_4$	$Fe^+_{Mg_{tet}}$	0.78	3.88[a]	1.93	1.74	0.19	3.44 (4.31) [12]	1.72 [62]
$ZnGa_2O_4$	$Fe^+_{Zn_{tet}}$	0.79	3.78[a]	1.92	1.71	0.21	3.54 (4.35) [59]	1.72 [63]
Inverse spinel								
$LiGa_5O_8$	$Fe^0_{Ga_{tet}}$	0.79	4.11[a]	1.75	1.70	0.05		1.84 [64,65]
	$Fe^0_{Ga_{oct}}$	1.86		1.03	0.76	0.27		~~1.01~~ [14]
$LiAl_5O_8$	$Fe^0_{Al_{tet}}$	0.89	4.02[a]	1.72	1.69	0.05	3.54 (4.09) [66,67]	1.70–1.80 [64,67,68]
	$Fe^0_{Al_{oct}}$	1.95		0.89	0.63	0.26		
Mg_2SnO_4	$Fe^0_{Mg_{tet}}$	0.73	3.91[a]	1.77	1.65	0.12	3.54 (4.13) [8]	1.72 [60]
Garnet								
YAG	$Fe^0_{Al_{tet}}$	0.85	4.30[a]	1.71	1.54	0.18	4.13 (4.43) [69,70]	1.58 [69]
	$Fe^0_{Al_{oct}}$	1.77		1.15	0.94	0.21		
	$Fe^0_{Y_{dod}}$	1.00		1.37	1.19	0.18		
YGG	$Fe^0_{Ga_{tet}}$	0.82	4.22[a]	1.72	1.50	0.22	4.13 (4.43) [70]	1.54 [70]
	$Fe^0_{Ga_{oct}}$	1.69		1.27	1.03	0.24		1.28–1.32 (Abs) [b] [71]
LuGG	$Fe^0_{Ga_{tet}}$	0.85	4.27[a]	1.68	1.46	0.22	4.13 (4.43) [70]	1.50 [70]
Perovskite								
$CaSnO_3$	$Fe^-_{Sn_{oct}}$	1.46	3.49[c]	1.32	1.18	0.14	3.54 (4.13) [17]	1.23 [17]
Ca_2InSbO_6	$Fe^0_{In_{oct}}$	1.25	3.52[a]	1.42	1.29	0.13	3.10 (3.59) [17]	1.33 [17]
	$Fe^{2-}_{Sb_{oct}}$	1.52		1.21	1.06	0.15		
Sr_2InSbO_6	$Fe^0_{In_{oct}}$	1.13	3.37[a]	1.47	1.36	0.11	3.10 (3.59) [17]	1.40 [17]
	$Fe^{2-}_{Sb_{oct}}$	1.49		1.24	1.10	0.14		
Ca_2ScSbO_6	$Fe^0_{Sc_{oct}}$	1.30	3.53[a]	1.38	1.26	0.12		
Sr_2ScSbO_6	$Fe^0_{Sc_{oct}}$	1.17	3.34[a]	1.46	1.35	0.11		
Zircon								
$ScPO_4$	$Fe^0_{Sc_{dod}}$	0.57	3.19[a]	2.07	1.97	0.10	3.10 (4.07) [72]	1.85 [72]
$LuPO_4$	$Fe^0_{Lu_{dod}}$	0.51	2.88[a]	2.15	1.76	0.39	2.85 (3.65) [72]	1.51 [72]
YPO_4	$Fe^0_{Y_{dod}}$	0.45	2.65[a]	2.12	1.68	0.47	2.79 (3.55) [72]	1.48 [72]
Others								
GaN	$Fe^0_{Ga_{tet}}$	1.00	2.89[a]	1.43	1.33	0.10		1.30 (ZPL) [3]
InP	$Fe^0_{In_{tet}}$	0.75	1.23[a]	0.44	0.40	0.04		0.53 (ZPL) [3]
ZnO	$Fe^+_{Zn_{tet}}$	0.86	3.27[a]	1.82	1.72	0.10		1.79 (ZPL) [73,74]
ZnS	$Fe^+_{Zn_{tet}}$	0.68	1.11[a]	0.83	0.78	0.05		1.01 [3]
$CuAlS_2$	$Fe^+_{Al_{tet}}$	0.64	0.76[a]	0.59	0.50	0.09	(1.29) [75]	0.72 (ZPL) [75]
$KMgF_3$	$Fe^+_{Mg_{oct}}$	1.64	5.18[a]	2.12	1.61	0.51		1.77 (ZPL) [76]
$CsCdCl_3$	$Fe^+_{Cd_{oct}}$	1.19/1.31		1.10/1.07	0.81/0.72	0.29/0.35		~~2.19~~ [77]
	$Mn^0_{Cd_{oct}}$	0.72/0.83		2.21/2.07	2.03/1.85	0.18/0.22		2.19 [77]

[a] $Fe^{3+} \rightarrow Fe^{2+} + h_{VBM}$ charge transfer transition.

[b] Experimentally observed absorption energy.

[c] $Fe^{3+} \rightarrow Fe^{4+} + e_{CBM}$ charge transfer transition.

Actually, it is natural that increased pressure leads to reduction in lattice constants and bond lengths and thus increased ligand field strength, and as a result, decreased emission energy of Fe^{3+} at the tetrahedral site. To verify this, we have calculated the pressure dependence of emission energy of the tetrahedral site in β phase, and obtained a rate of -57 cm^{-1}/GPa (refer to Fig. S10 of the Supplemental Material [47] for detailed data), not so far from the reported rate of -74 cm^{-1}/GPa,

considering its large uncertainty of experimental data. Hence, we attribute the pressure-dependent emission to a tetrahedral Fe^{3+} site, either from β-$LiGaO_2$ or a disorder phase.

B. Iron in garnets—More tetrahedral coordinated Fe^{3+} luminescence cases

Garnets are well known systems, and the electron-phonon coupling of Fe^{3+} has been an important field of research unto

itself, particularly in reference to YIG, where the Fe ion is part of the host matrix instead of a dopant [87,88]. In this study, we examine the site occupancy, valence states, and optical transitions of iron dopants in garnets. The garnet crystal belongs to the space group $Ia\bar{3}d$ (No. 230) with the stoichiometric formula $A_3B_2B'_3O_{12}$, where A, B, and B′ coordinate oxygen atoms dodecahedrally, octahedrally and tetrahedrally with D_2, C_{3i}, and S_4 point symmetry, respectively, as shown in Fig. 1(c). In our work, we systematically study the variation trends of energy levels and photoluminescent properties of Fe^{3+} in a series of garnet hosts, including $Y_3Al_5O_{12}$ (YAG), $Y_3Ga_5O_{12}$ (YGG), $Lu_3Ga_5O_{12}$ (LuGG), using first-principles calculations.

Taking the YAG garnet host as an example, we analyzed the site-occupancy and valence states of iron dopants in garnets through defect formation energy calculations, as shown in Fig. 1(f). We used the chemical-potential condition of equal formation enthalpy to raw materials, i.e., $\Delta\mu_{Y_2O_3} = \Delta H^f_{YAG}/3$, and $\Delta\mu_{Al_2O_3} = \Delta H^f_{YAG}/5$. Then, the chemical potentials of host-related elements can be determined under the condition of $\Delta\mu_O = -1.3$ eV. The value of μ_{Fe} is determined by the doping concentration, subject to the constraints set by all Fe-related compounds. Since the intrinsic defects exhibit high formation energies, E^0_F is dominantly determined by the formation energy functions of iron substitution defects, specifically the dominant positively charged $Fe^+_{Al_{oct}}$ or $Fe^+_{Al_{tet}}$, and the dominant negatively charged $Fe^-_{Y_{dod}}$. At this E^0_F, the neutrally charged defect $Fe^0_{Al_{oct}}$ (Fe^{3+}_{oct}) and $Fe^0_{Al_{tet}}$ (Fe^{3+}_{tet}) are the most abundant in defect concentrations. Adjusting the chemical potentials can hardly tune the site occupancy and valence states of iron dopants (see more details in Note 2 of the Supplemental Material [47]). Similarly, the iron dopant in YGG and LuGG hosts also can occupy the octahedral and tetrahedral sites and mainly show Fe^{3+} valence states.

Next, we calculate the optical transitions of three types of iron substitutions in YAG host. The ligand field strengths of Fe^{3+} at the three types of sites follow the order: $\Delta_{oct} > \Delta_{dod} > \Delta_{tet}$, and the predicted emission energies follow the trend: $Fe^{3+}_{tet} > Fe^{3+}_{dod} > Fe^{3+}_{oct}$. The experimentally observed emission at approximately 785 nm [69] and the ZPL of approximately 1.63 eV (760 nm) in the YAG host [89] can be attributed to the tetrahedral Fe^{3+}, and the calculated emission energy aligns well with experimental results. The calculated emission energies of Fe^{3+} in a series of garnets follow the trend: YAG > YGG > LuGG. The experimentally observed emissions in these hosts fall within the range of 770–830 nm [70], which align well with the calculated emission energies of tetrahedral coordinated Fe^{3+}. Additionally, the $^4A_1/^4E$ excited state is calculated to be 2.36 eV relative to $^6A_1$ ground state based on the occupation matrix control methodology [55]. This value slightly underestimates the experimentally observed $^6A_1 \rightarrow {}^4A_1/{}^4E$ transition energy of about slightly over 2.50 eV by near 0.2 eV, a reminiscent trend of the underestimation in the calculated $^4A_1/^4E$ excited states of tetrahedral Mn^{2+} in solids [55]. The calculated Racah parameters B of Fe^{3+}_{tet} in garnets exhibit remarkable consistency. Specifically, the values are 0.069 eV in YAG and YGG, and 0.07 eV in LuGG host, indicating their close proximity within these garnets.

Besides, the absorption spectra of Fe^{3+} in YGG crystal were extensively studied [87]. The peak absorption energy of $^6A_1 \rightarrow {}^4T_1$ is reported to be approximately 1.28 eV in experiments. The ligand field strength, determined by fitting from the absorption spectra, is 1.62 eV for $Fe^0_{Ga_{oct}}$ (Fe^{3+}_{oct}) and 0.81 eV for $Fe^0_{Ga_{tet}}$ (Fe^{3+}_{tet}). Our calculations, based on the multiplicity control method with the hybrid functional, yield an absorption energies of $^6A_1 \rightarrow {}^4T_1$ of 1.25 eV, which aligns well with the experimental results of 1.28 eV. The calculated ligand field strengths for $Fe^0_{Ga_{oct}}$ (Fe^{3+}_{oct}) and $Fe^0_{Ga_{tet}}$ (Fe^{3+}_{tet}) are 1.69 and 0.82 eV, respectively, which are calculated by the equal occupancy at five $3d$ orbitals with spin unpolarized GGA and $U = 0$ calculations [55]. However, no emission has been reported experimentally for these octahedral Fe^{3+}, and this will be interpreted in Sec. III C.

It is important to note that the predicted emission energy of $Fe^0_{(Al/Ga)_{oct}}$ (Fe^{3+}_{oct}) in garnets is about 0.3 eV higher than that of $Fe^0_{(Al/Ga)_{oct}}$ in spinel-type host. This originates from the facts that the ligand field strength of Fe^{3+}_{oct} in garnets is smaller than that in spinel-type host, while the Coulomb interaction parameter B in garnets is larger. A similar phenomenon has been observed for Mn^{3+}. In spinel hosts, the $^1T_2$ excited states are much lower than $^5T_2$ of Mn^{3+}_{oct}, which lead to the near-infrared $^1T_2 \rightarrow {}^3T_1$ emission [91,92]. However in garnet hosts, the $^1T_2$ excited states are comparable with $^5T_2$ of Mn^{3+}_{oct}, which leads to the temperature dependent red ($^5T_2 \rightarrow {}^5E'$) and near-infrared ($^1T_2 \rightarrow {}^3T_1$) emissions [93,94].

Finally, the luminescence with band peak ranging from 670 to 830 nm has been widely reported in iron-doped crystals, which can be attributed to the optical transitions of tetrahedral Fe^{3+}. For a systematic discussion, the optical transitions and local structures of tetrahedrally coordinated Fe^{3+} activators in a variety of hosts are listed in Table II. Some typical cases such as iron-doped spinels and garnets have been calculated, with results aligning with the experiments (refer to Fig. S12 in the Supplemental Material [47] for detailed comparison). Considering that multiplet sites and hosts are involved, and to avoid errors in calculations, we have used the experimentally observed emission energies instead, and the bond lengths and bond angles are based on the ground-state calculations after iron substitution. Generally, Fe^{3+} ions favor replacing Mg^{2+}, Zn^{2+}, Ga^{3+}, and Al^{3+} at tetrahedral sites where the ion radius difference is less than or about 0.10 Å. The change of bond length for iron substitution follows the difference in ion radius between Fe^{3+} and the ion being replaced, with a ratio about 0.83 (see more details in Fig. S11 of the Supplemental Material [47]), leading to very close Fe^{3+}–O bond lengths in different hosts (Table II). For the counterpart of octahedral site, Fe^{3+} replaces an ion with radius from about 0.10 Å smaller to about 0.16 Å larger, but the ratio of the change in bond length to that in ion radius is about 0.69. Both the ratios 0.83 and 0.69 are larger than the value of 0.60 for various ion substitution [54]. The standard deviation of the angular distortion and emission energy of each site is also listed in Table II, which shows an overall correlation between the decrease in emission energy and the increase in angular distortion.

Moreover, it is worth mentioning that some of us have previously investigated the luminescence of iron ions in

TABLE II. Average bond length ($\bar{L}$) in units of Å and standard deviation of bond angles [$\sigma(A)$] in units of degrees for Fe^{3+} substituted at tetrahedral M site with surrounding coordinations ($[FeO_4]$) in host crystals.

	$MgAl_2O_4$	$ZnAl_2O_4$	Li_2ZnSiO_4	Li_2ZnGeO_4	$LiGa_5O_8$	$LiAl_5O_8$	$LiGAO_2$	YAG	YGG	LuGG
M_{tet}	Mg	Zn	Zn	Zn	Ga	Al	Ga	Al	Ga	Ga
$\bar{L}(M–O)$	1.96	1.98	1.99	1.99	1.87	1.79	1.86	1.78	1.87	1.86
$\bar{L}(Fe^{3+}–O)$	1.89	1.89	1.91	1.91	1.89	1.88	1.88	1.86	1.88	1.86
$\sigma[A(O–Fe^{3+}–O)]$	0.16	0.15	2.24	6.62	0.17	0.81	1.83	7.96	8.60	8.83
Expt. emi.	1.73	1.76	1.65 [90]	1.60 [90]	1.68	1.71	1.66	1.58	1.54	1.50

	$CaGa_2O_4$				$CaAl_2O_4$					
M_{tet}	Ga1	Ga2	Ga3	Ga4	Al1	Al2	Al3	Al4	Al5	Al6
$\bar{L}(M–O)$	1.87	1.87	1.88	1.86	1.77	1.78	1.77	1.78	1.78	1.77
$\bar{L}(Fe^{3+}–O)$	1.89	1.87	1.89	1.90	1.87	1.87	1.87	1.87	1.87	1.87
$\sigma[A(O–Fe^{3+}–O)]$	9.35	6.08	13.46	12.71	9.16	6.63	6.79	4.68	4.25	7.83
Expt. emi.		1.53 [61]				1.57 [61]				

$MAl_{12}O_{19}$ (M = Ca, Sr, Ba) and clarified that some certain emissions are from Fe^{3+}, rather than from Bi^{3+} [9]. These investigations employed first-principles calculation of formation energy as well as excited-state processes. The luminescence observed at approximately 1.5 eV has been unequivocally attributed to Fe^{3+} ions occupying a five-coordinate site, resulting in the formation of a rigid trigonal bipyramid structure for M = Ca and Sr, while for M = Ba, a tetrahedral site perturbed by an additional oxygen site further away was identified [9].

C. Iron in Perovskites—Luminescence from Fe^{3+} at octahedral sites

Recently, efficient near-infrared emissions have been reported in Fe^{3+}-activated perovskite ABO_3 and double perovskite $A_2B'B''O_6$ [17], where A, B, B′, and B″ are divalent, tetravalent, trivalent, and pentavalent ions, respectively. In this section, we aim to determine the site occupancies, and excitation and emission transition energies of iron ions in perovskites using first-principles calculations.

First, we determined the main intrinsic defects by calculating their formation energies. The results are plotted in Fig. 2. For the $CaSnO_3$ host, we applied a chemical potential condition that equally distributes the formation enthalpy to binary oxides, i.e., $\Delta\mu_{CaO} = H^f_{CaSnO_3}/2$, $\Delta\mu_{SnO_2} = H^f_{CaSnO_3}/2$, and employs the usual sintering atmosphere $\Delta\mu_O = -1.3$ eV. In the absence of any impurities, the dominant intrinsic defects are the antisite defects Ca^{2-}_{Sn} and Sn^{2+}_{Ca}. The Fermi energy E^0_F is estimated from the intersection of the formation energy curves of these two antisites with opposite charge states. When iron is introduced into the system, the chemical potential μ_{Fe} is determined using a replacement ratio of 0.05% as a reference. The formation energy of iron substitution at an octahedrally coordinated site is much smaller than that at a dodecahedral coordinated site. This leads to the concentration of the former dominating over the latter. In this scenario, E^0_F is determined by the dominant positively charged defect Sn^{2+}_{Ca} and the dominant negatively charged defect Fe^-_{Sn}. For the Ca_2InSbO_6 quaternary compound, the phase diagram and permissible chemical potentials can be studied through the coexistence of ternary or binary compounds [95]. We

apply the chemical-potential condition of coexistence with In_2O_3 and $Ca_2Sb_2O_7$ phases, i.e., $\Delta\mu_{In_2O_3} = 0$, $\Delta\mu_{Sb_2O_5} = 2H^f_{Ca_2Sb_2O_7} - 2H^f_{Ca_2InSbO_6}$, $\Delta\mu_{CaO} = H^f_{Ca_2InSbO_6} - H^f_{Ca_2Sb_2O_7}/2$, and $\Delta\mu_O = -1.3$ eV. Our calculations reveal that the defect concentrations of intrinsic antisites In^{2-}_{Sb} and Sb^{2+}_{In} dominate over others. The Fermi energy E^0_F is estimated by the intersection of the formation energies of these two defects with opposite charge states. At this E^0_F, iron can substitute at both B′ and B″ octahedral coordinated sites to form Fe^0_{In} and Fe^{2-}_{Sb}. Compared with Fe^{2-}_{Sb}, the formation energy of Fe^0_{In} is smaller and thus its concentration is larger. The effects of tuning chemical potentials on the site occupancy and valence states of iron in perovskites are discussed in Note 2 of the Supplemental Material [47]. It shows that iron dopants mainly substitute at octahedral coordinated Sn^{4+} or In^{3+} sites and appear as Fe^{3+} in all the possible chemical-potential ranges.

In the $CaSnO_3$ host, Fe^-_{Sn} (Fe^{3+}_{oct}) is dominant in concentration, accounting for the experimentally observed near-infrared emission [17]. The ligand field strength is calculated and found to be significantly smaller than that of Fe^{3+} at octahedral Al^{3+} sites or Ga^{3+} sites in spinel, inverse spinel and garnet systems. This is due to the much larger bond length when Fe^{3+} replaces Sn^{4+}, which has a relatively larger ionic radius than Al^{3+} or Ga^{3+}. As a result, the emission energy of Fe^{3+} at octahedral Sn^{4+} site is predicted to be larger than that of Fe^{3+} at octahedral Al^{3+} or Ga^{3+} sites in spinel-type and garnet crystals. In the Ca_2InSbO_6 double perovskite, there are two possible sites for Fe^{3+} occupancy. The larger radius of In^{3+} than Sb^{5+} results in a longer average bond length and consequently a weaker ligand field of Fe^0_{In} than Fe^{2-}_{Sb}. Thus, the emission energy of Fe^0_{In} is predicted to be larger than that of Fe^{2-}_{Sb}. The same situation applies to the Sr_2InSbO_6 host. The experimentally observed emission in both the $(Ca/Sr)_2InSbO_6$ hosts is attributed to Fe^0_{In} (Fe^{3+}_{oct}) because it is dominant in concentration and its emission energy is close to that observed experimentally (refer to Table I or Fig. S12 in the Supplemental Material [47] for a detailed comparison). The NIR emission energies of Fe^{3+} are predicted to increase along with $CaSnO_3$, Ca_2InSbO_6, and Sr_2InSbO_6.

Luminescence similar to these octahedral Fe^{3+} has been reported in Sc-based $NaScSi_2O_6$ host and another double-
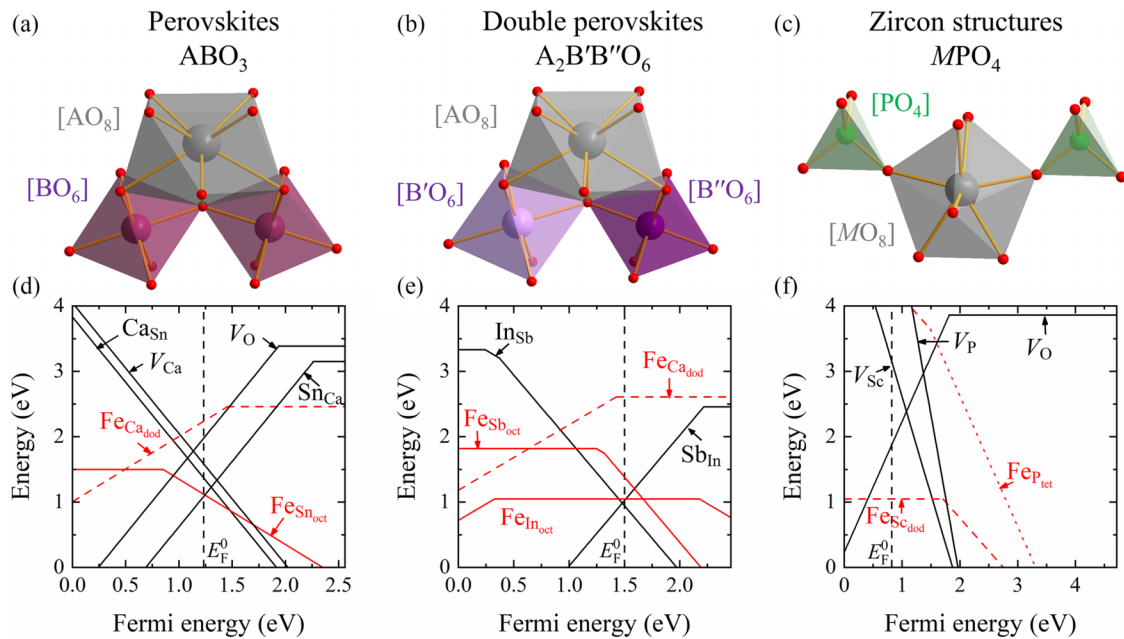
FIG. 2. (a)–(c) Local octahedron and dodecahedron structures of ABO_3 perovskites, $A_2B'B''O_6$ double perovskites, and MPO_4 zircon structures. (d)–(f) Formation energies of dominant defects in $CaSnO_3$ and Ca_2InSbO_6 perovskite and $ScPO_4$ zircon structure hosts, respectively.

perovskite system $CaLaMgSbO_6$. An experimental study on iron-doped $NaScSi_2O_6$ crystal reported a broadband near-infrared emission peaking at 900 nm [96]. Our calculations suggest that the iron impurity can occupy the octahedrally coordinated Sc^{3+} site in this host, and the emission energy of octahedral Fe^{3+} is calculated as 1.39 eV, aligning well with the experimental result. In $CaLaMgSbO_6$ host, Fe^{3+} ions preferentially occupy Mg^{2+} sites due to the small differences in charge and ionic radius. The high-efficient NIR emissions centered at 995 nm was reported in experiments, and the $^4T_1 \rightarrow {}^6A_1$ emission is calculated to be 1.25 eV. It should be noted that the calculated emissions of octahedral coordinated Fe^{3+} are systematically underestimated relative to the experiments by about or less than 0.05 eV.

The observed Fe^{3+}-related photoluminescence in $(Ca, Sr)_2InSbO_6$, $CaLaMgSbO_6$, $CaSnO_3$, and $NaScSi_2O_6$ hosts can be attributed to Fe^{3+} occupying the octahedral coordinated In^{3+}, Mg^{2+}, Sn^{4+} or Sc^{3+} sites. However, no photoluminescence has been confirmed for the octahedral coordinated Fe^{3+} in the spinel and garnet hosts studied above, although the appearance of absorption of octahedral coordinated Fe^{3+} in YGG has been observed [87]. Note that $Fe^{2+} + h_{VBM}$ or $Fe^{4+} + e_{CBM}$ charge-transfer excited states are all about 2 eV higher than $^4T_1$ excited states, so the luminescence quenching via charge-transfer transition or photoionization process is negligible. Generally, larger gap between the excited and ground state, weaker electron-phonon coupling and smaller phonon frequencies favor the luminescence, while small activation energies between the excited state and ground state, and the presence of quenching center can lead to thermal and concentration quenching of luminescence. To further understanding these phenomena, the configuration coordinate diagrams of Fe^{3+} are constructed by choosing $MgAl_2O_4$ and Ca_2InSbO_6 as representatives, which are depicted in Fig. 3. The configuration coordinate diagrams

are constructed by linearly interpolating the coordinates between the equilibrium geometric structures of $^6A_1$ ground and $^4T_1$ excited states. The energies of $^6A_1$ ground state, $^4T_1$ and $^4A_1 / {}^4E$ excited states are calculated at each structure point. Note that the lattice displacements of $^4T_1$ relative to $^6A_1$ is dominated by the e-type Jahn-Teller distortion combined with A_{1g} systematic compression, while that of $^4A_1 / {}^4E$ should be mainly dominated by A_{1g}-type systematic compression [55]. The configuration coordinate is defined with

$$Q^2 = \sum_a m_a \left| \left(\mathbf{R}_a^f - \mathbf{R}_a^i \right) \right|^2, \qquad (6)$$

where α denotes the atom, m is atomic mass, and R are the atomic coordinates with f and i for equilibrium geometric structures of interpolated and ground states, respectively. The solid lines are quadratic fittings to calculated energies. We failed to obtain the energies of $^4A_1 / {}^4E$ by the constraint occupancy method, as the occupancies always switched to those of $^4T_1$ with lower energies during the calculation of Kohn-Sham orbitals. As a compromise, we estimated the $^4A_1$ excited-state energy of Fe^{3+} with $E(^4A_1 - {}^6A_1) \approx 10B + 5C$ and $E(^4T_1 - {}^6A_1) \approx 10B + 6C - 10Dq$ by using the calculated $E(^4T_1 - {}^6A_1)$, $10Dq$, and $C/B = 4.73$. The result is depicted as dashed blue curve parallel to that of the ground state in Fig. 3. For comparison, the excitation energy of $^4A_1 / {}^4E$ in iron-doped YGG crystal is 2.50–2.52 eV for the tetrahedral site and 2.56–2.62 eV for the octahedral site [87]. It is worth pointing out that the C/B ratio can differ quite substantially between tetrahedral and octahedral sites by fitting experimental data, as $C/B = 3.44$ and 5.85 were obtained for tetrahedral and octahedral Fe^{3+} sites in YGG host [87]. Nonetheless, such ratios only lead to an increase of 0.03 eV and a decrease of 0.02 eV in the estimated $^4A_1 / {}^4E$ energies for tetrahedral and octahedral Fe^{3+} in the $MgAl_2O_4$ host, respectively.
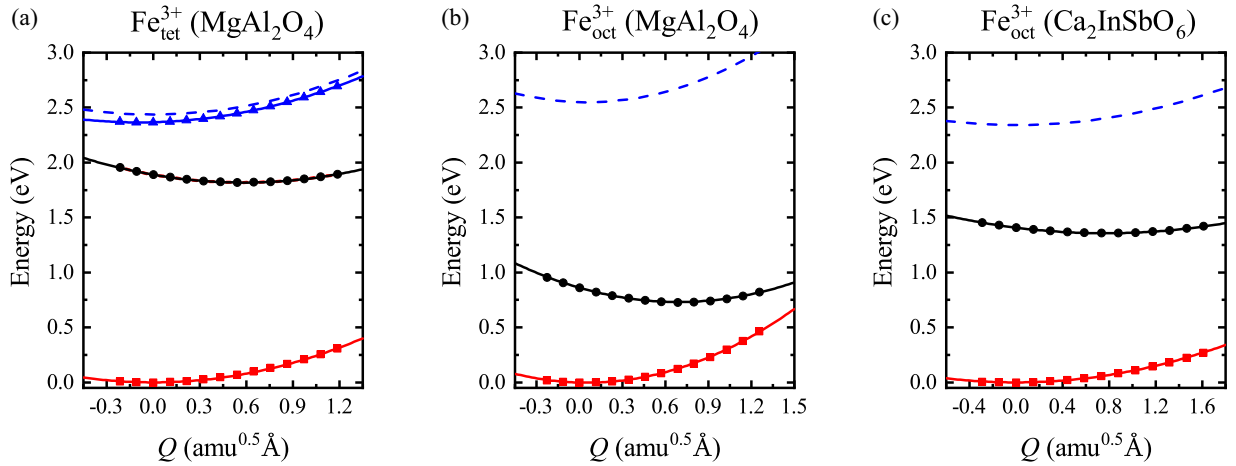
FIG. 3. Configuration coordinate diagrams of $^6A_1$ ground state (red square points and lines), $^4T_1$ (black circle points and lines), and $^4A_1 / ^4E$ (blue triangle points and lines) excited states of Fe^{3+}: (a) at tetrahedral-coordinated Mg^{2+} site, (b) at octahedral-coordinated Al^{3+} site in $MgAl_2O_4$ host, and (c) at octahedral coordinated Sb^{3+} site in Ca_2InSbO_6 host. Other excited states, such as $^4T_2$, are not included because the potential emission state is $^4T_1$. It should be noted that Q is defined with Eq. (6) and takes positive value alone the lattice displacement from the $^6A_1$ ground state to the $^4T_1$ excited state. The red, black, and blue solid lines are fitted according to the calculated $^6A_1$, $^4T_1$, and $^4A_1 / ^4E$ points. The blue dashed lines represent deduced $^4A_1 / ^4E$ excited states with $E(^4T_1 - {}^6A_1)$, $10Dq$, and C/B values as detailed in the text.

From Fig. 3, it can be observed that the ratio of Dq/B increases in the order of Fe_{tet}^{3+} ($MgAl_2O_4$), Fe_{oct}^{3+} (Ca_2InSbO_6), Fe_{oct}^{3+} ($MgAl_2O_4$), as indicated by the increase in energy difference between $^4A_1 / ^4E$ and $^4T_1$ excited states. The activation energy of the $^4T_1$ state of Fe^{3+} at octahedral coordinated Al^{3+} site in $MgAl_2O_4$ host is estimated as about 0.4 eV. This is significantly smaller due to the low transition energy and large Stokes shift than that of Fe_{tet}^{3+} in $MgAl_2O_4$ and that of Fe_{oct}^{3+} in Ca_2InSbO_6 host with about 6.1 and 2.2 eV, respectively. The potential luminescence from $^4T_1$ after excitation and relaxation is assessed using the Dexter-Klick-Russell parameter [97], defined as $\Lambda = (1/2)(E_S/E_{abs})$, with E_S and E_{abs} corresponding to the Stokes shift and the absorption peak energy of $^6A_1 \leftrightarrow {}^4T_1$ transition, respectively. An increase in Λ value tends to favor the quenching of luminescence. The calculated Λ values for Fe^{3+} are 0.037, 0.122, and 0.046 for Fe^{3+} at tetrahedral coordinated Mg^{2+} site in $MgAl_2O_4$, octahedral coordinated Al^{3+} site in $MgAl_2O_4$, and octahedral coordinated Sb^{3+} site in Ca_2InSbO_6 hosts, respectively. These values indicate that Fe_{oct}^{3+} in $MgAl_2O_4$ is less-likely than Fe_{tet}^{3+} in $MgAl_2O_4$ and Fe_{oct}^{3+} in Ca_2InSbO_6 to produce luminescence. A similar small Λ_M value of about 0.1 has been reported for Mn^{2+} in solids, which is qualitatively related to the low radiative decay rate of Mn^{2+} [98]. As listed in Table I, the octahedral Fe^{3+} of these perovskites are more favorable for luminescence, as indicated by their Λ values, compared with those in spinels and garnets. This is because the former systems not only exhibit much smaller Stokes shifts (about 50% of the latter) but also have higher excitation energies.

As a prediction, we have also done the calculations for the iron-doped double perovskites $(Sr, Ca)_2ScSbO_6$. Our defect formation energy calculations indicate that iron ions mainly occupy the octahedrally coordinated Sc^{3+} site as Fe^{3+} valence states (refer to Fig. S8 in the Supplemental Material [47] for detailed data). The predicted emission energies of Fe_{Sc}^0 (Fe_{oct}^{3+}) in $(Sr, Ca)_2ScSbO_6$ are 1.35 and 1.26 eV, respectively, which are close to that of Fe_{In}^0 in $(Sr, Ca)_2InSbO_6$

hosts. The Λ values of Fe^{3+} at the octahedral coordinated Sc^{3+} site in $(Sr, Ca)_2ScSbO_6$ are comparable to those at the octahedral In^{3+} site in $(Sr, Ca)_2InSbO_6$, suggesting potential luminescence.

D. Hosts with zircon structure—Luminescence from dodecahedral coordinated Fe^{3+}

Red emissions have been reported in iron-doped MPO_4 (M = Sc, Lu, Y) crystal, with a luminescent decay time about 1 ms and the thermal quenching temperatures ranging from 100 to 200 K, depending on the ion M [72]. These zircon-structured MPO_4 hosts crystallize with $I4_1/amd$ space group, which consists of chains of alternating PO_4 tetrahedra and MO_8 units. The M and P atoms are dodecahedrally and tetrahedrally coordinated, respectively, with D_{2d} point groups.

Our calculations reveal that within the permissible chemical-potential range, iron dopants tend to occupy the dodecahedral M site and iron substitution at the tetrahedral P site requires an enormously larger formation energy. The formation energies of iron dopants and intrinsic defects as the function of Fermi energy in the chemical-potential condition $\Delta\mu_{Sb_2O_3} = H_{ScPO_4}^f$, $\Delta\mu_{P_2O_5} = H_{ScPO_4}^f$, and $\Delta\mu_O = -1.3$ eV are shown in Fig. 2. The Fermi energy E_F^0 can be estimated by the intersection of formation energies of the dominant positively charged V_O^{2+} defect and dominant negatively charged $Fe_{Sc_{dod}}^-$ defect. At this E_F^0, the formation energy of $Fe_{Sc_{dod}}^0$ (Fe^{3+}) is significantly lower than that of $Fe_{P_{tet}}^{2-}$.

Next, we examined the optical transitions of Fe^{3+} situated at the dodecahedral site in these zircon structures. The charge-transfer excitations, which are of high intensity, exhibit a large width. The onset of these excitations in iron-doped $ScPO_4$, $LuPO_4$, and YPO_4 hosts are 3.10, 2.85, and 2.79 eV, respectively. Our calculations indicate that the $Fe^{3+} \rightarrow Fe^{2+} + h_{VBM}$ excitations are correspondingly 3.19, 2.88, and 2.65 eV, which aligns with the experimental trend [72]. The calcu-

lated Stokes shifts for the $^6A_1 \rightarrow {}^4T_1$ transition of Fe_{dod}^{3+} in ScPO$_4$, LuPO$_4$, and YPO$_4$ hosts are 0.10, 0.39 and 0.45 eV, respectively. These values align with the trend observed in the experimental results, which are 0.06, 0.25, and 0.28 eV, respectively. In addition, the calculated emission energies are 1.97, 1.76, and 1.68 eV, respectively, while the corresponding experimental energies are 1.85, 1.51, and 1.48 eV. It is worth noting that the calculated emissions of dodecahedral coordinated Fe^{3+} in zircon structures systematically overestimate the experimental values by about 0.2 eV (refer to Fig. S12 in the Supplemental Material [47] for detailed comparison).

It is worth noting that our calculations were carried out with the constrained spin multiplicity method in the density functional theory. In this method, the $^4T_1$ excited states are approximated as the $|\xi\eta\bar{\epsilon}\theta\epsilon|$ Slater determinant, and the mixing (configuration interaction) between different Slater determinants due to Coulomb interactions is disregarded, which alone would lead to an increasing overestimation in calculations as the ligand field strength decreases. In cases where the ligand field strength is small, about 0.5 eV, this overestimation plays a significant role and leads to an overestimation of the energy from the single Slater determinant relative to the exact $^4T_1$ excited states, although part of such overestimation will be offset by the spin contamination underestimation. Furthermore, dodecahedral coordinations of Fe^{3+} in phosphates exhibit significant distortion from standard cubic structure, and the mixing due to Coulomb interaction between different single Slater determinants of $^4T_1$ will be larger. As a result, the calculated transition energies overestimate by about 0.2 eV compared with experimental results. However, in cases of relatively larger ligand field strength, the calculation results align with experimental values. It is worth noting that other errors, such as overestimation of the Coulomb parameters B, underestimation of the crystal-field parameters, or metastable excited state structures without sufficiently relaxation, can also lead to overestimation of the emission energies.

Furthermore, the ligand field strength of Fe^{3+} at dodecahedral Y^{3+} site in YPO$_4$ host is significantly smaller, about half of that in the YAG host. This can be attributed to the subspherical distribution of coordinated oxygen ions in YPO$_4$, in contrast with the distorted cubic distribution in YAG host. For comparison, we derived the ligand field strength from the effective ligand-field splitting, yielding values 0.57, 0.51, 0.45, and 1.00 eV for ScPO$_4$, LuPO$_4$, YPO$_4$, and YAG, respectively. Additionally, the ligand-field splitting calculated by the differences of the highest and lowest d orbital energies are 0.88, 0.76, 0.67, and 1.46 eV of Fe$_{dod}^{3+}$ in ScPO$_4$, LuPO$_4$, YPO$_4$, and YAG hosts with spin-unpolarized calculations, respectively. Additionally, the Racah parameters B of Fe$_{dod}^{3+}$ are calculated to be 0.078 eV in ScPO$_4$, LuPO$_4$, and YPO$_4$ hosts, larger than that in YAG host of 0.069 eV. The larger Racah parameter B and thus consequently smaller nephelauxetic effects of Fe^{3+} in phosphates can be attributed to the reduced covalent bonding between cation and anion ligands. This is similar to the case of the Bi^{3+}, whose $6p \rightarrow 6s$ emission energy is much larger of around 5 eV in phosphates than around 3–4 eV in many other oxides [99]. Consequently, for Fe^{3+} occupying a dodecahedral site, the Dq/B value is much smaller, and as a result, the predicted emission energy is much larger in phosphates than

that in the YAG host. It is worth noting that the emission energies of dodecahedral Fe^{3+} decrease along ScPO$_4$, LuPO$_4$, and YPO$_4$ hosts, which can be attributed to the increased excited-state structural distortion relaxation from Sc to Y due to the progressively larger mismatch in ionic radius.

E. Iron in other hosts—Luminescence from Fe^{3+} in semiconductors and halides

Iron impurities in III-V and II-VI semiconductors have been extensively studied experimentally [3,19,74]. Much of the research focuses on the deactivation process, and it is crucial to clarify the nephelauxetic effects of Fe^{3+} in different hosts with various anion ions, and elucidate the competition of different excited states and the radiative and nonradiative processes. The impact of Fe^{3+} and its interplay with other impurities on the optical properties has been studied in the group-III nitride semiconductors [1]. Here, we analyze the ligand field strength, nephelauxetic effects, excited states and optical transitions of Fe^{3+} in the semiconductors with different anions, including GaN, InP, ZnO, ZnS, and CuAlS$_2$.

Calculations on formation energies show that iron impurities replacing cation ions primarily exhibit Fe^{2+} and Fe^{3+} valence states in these hosts. The optical transition energies of Fe^{3+} substituted at cation sites are listed in Table I. The transition energy of Fe^{3+} decreases along ZnO, GaN, ZnS, and InP hosts. The calculated transition energy of Fe^{3+} in GaN agrees well with the experimental value, while that in the InP host underestimates the experimental value by about 0.1 eV. This underestimation is attributed to the overestimation of hybridization of Fe-d with the P-p orbitals, the main composition of the upshifted valence band maximum. Similarly, the calculated transition energy of Fe^{3+} in ZnO agrees with the experiments, while that in sulfide hosts underestimates the experimental results by about 0.2 eV.

The emission energy of Fe^{3+} is governed not only by the nephelauxetic effect, but also the ligand field splitting of Fe-d orbitals. The ligand field strengths of Fe$_{tet}^{3+}$ are calculated by equal occupancy at five $3d$ orbitals in the band gap with spin unpolarized setting. The values are 1.00, 0.86, 0.75, and 0.68 eV for GaN, ZnO, InP, and ZnS hosts, respectively. The Racah parameters B are calculated by the $^4A_1/{}^4E$ excited states, and the values are 0.065, 0.059, 0.043, and 0.029 eV in ZnO, GaN, ZnS, and InP hosts, respectively. The reduction of B from its free ion value $1 - B/B_0$ is normally reported in terms of the nephelauxetic effect, which describes the covalent bonding between cation and anion ligands. The $1 - B/B_0$ values are separately calculated as 0.48, 0.53, 0.66, 0.77 for Fe^{3+} in ZnO, GaN, ZnS, and InP hosts, respectively. The B_0 value used for free Fe^{3+} is 1015 cm^{-1} [56]. Then, the $10Dq/B$ values can be obtained as 13.3, 16.9, 15.8, and 25.8 for ZnO, GaN, ZnS, and InP hosts, respectively. Therefore the emission energies decreases for Fe^{3+} in ZnO, GaN, ZnS, and InP hosts due to the combination of increased nephelauxetic effects and increased Dq/B. The emission energy is significant underestimated in ZnS and InP, implying that the nephelauxetic effect and the ratio of Dq/B may have been overestimated. In addition, the smaller B value of Fe^{3+} in CuAlS$_2$ of 0.036 eV than in ZnS (0.043 eV) has led to the smaller emission energy in CuAlS$_2$.
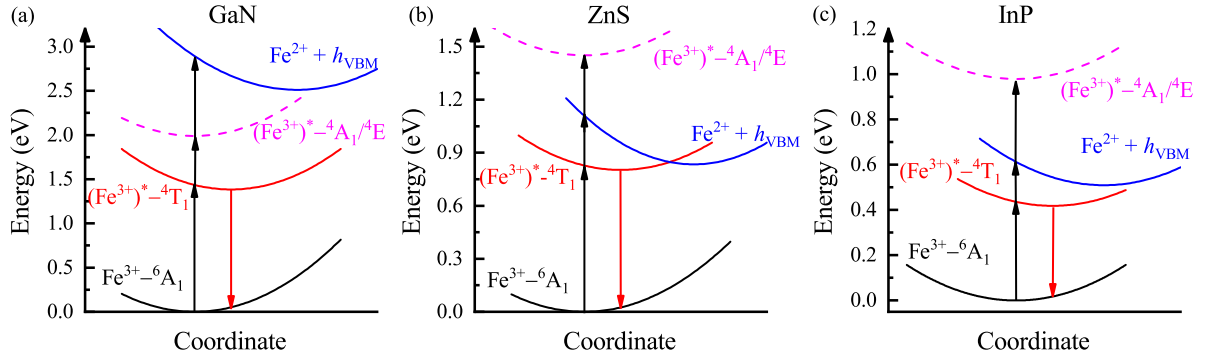
FIG. 4. Configuration coordinate diagrams of the ground states and different excited states of Fe^{3+} in (a) GaN, (b) ZnS, and (c) InP hosts.

Next, we discuss in detail the excited states and optical transition processes in detail by utilizing configuration coordinate diagrams constructed with calculated data for Fe^{3+} in the GaN [Fig. 4(a)], ZnS [Fig. 4(b)], and InP [Fig. 4(c)] hosts.

In the GaN host [Fig. 4(a)], the band gap calculated with HSE06 is 3.12 eV, which is underestimated compared with the experimental band gap of 3.50 eV [100]. The calculated thermal charge transition level $\varepsilon(0/-)$ is 2.46 eV above the VBM, and the calculated optical transition energy of Fe^{3+} $(Fe_{Ga}^0) \rightarrow Fe^{2+} + h_{VBM}$ $(Fe_{Ga}^- + h_{VBM})$ optical transition is 2.89 eV. It is worth noting that in the charge-transferred state, the holes are approximated as free holes, and the polarization of the polaron is neglected, leading to an overestimation in the meV scale [101]. Both values are slightly underestimated with respect to previous calculations [1]. This underestimation is attributed to the overestimation of the VBM, which is linked to the band-gap underestimation. In contrast, the onset of the experimental absorption spectra is observed at 2.86 eV in iron-doped GaN at low temperature [3]. The $^6A_1 \rightarrow {}^4A_1 / {}^4E$ excitation is calculated as 1.99 eV, aligning with the sharp peak observed at 2.00 eV [19]. Note that the energy difference $E(^4A_1 / {}^4E) - E(^6A_1)$ is due to Coulomb interaction, which is smaller in nitrides than that in oxides (≈ 2.5 eV in YGG [87]) as a result of the larger nephelauxetic effects in nitrides than in oxides. $^4T_1 \rightarrow {}^6A_1$ emission is calculated as 1.33 eV, close to the observed 1.30 eV zero-phonon line at low temperature [19,102].

In the ZnS host, the band gap calculated with HSE06 is 3.36 eV, which is underestimated when compared with the experimental value of 3.78 eV [100]. As depicted in Fig. 4(b), the position of $Fe^{2+} + h_{VBM}$, as estimated from the calculated thermal charge transition level $\varepsilon(+/0)$ of iron, is 0.88 eV over VBM, and the calculated optical transition $Fe^{3+} \rightarrow Fe^{2+} + h_{VBM}$ is 1.11 eV. Experimentally, the minimum energy required to excite an electron optically from valence band into the Fe^{3+} center was reported as about 1.4 eV [103] or 1.6 eV [104]. The energy required to ionize an electron from Fe^{2+} into conduction band was around or over 3.0 eV [103]. The sum of these two energies is larger than the band gap, with the additional amount to account for the two relaxations of the optical transitions. Note that the underestimated energy of $Fe^{3+} \leftrightarrow Fe^{2+} + h_{VBM}$ can be related to the underestimation of band gap, as the correction to band gap will mainly lead to downshift of valence-band maximum in these d^{10} semiconductors. The observed emission can be attributed to be from

$^4T_1$, which is underestimated by about 0.21 eV by comparing the calculated and experimental emission energies in Table I.

In the InP host, as depicted in Fig. 4(c), the optical excitation $Fe^{3+} \rightarrow Fe^{2+} + h_{VBM}$ is calculated to be 0.61 eV. This is compared with the experimentally reported photoionization threshold of about 0.77 [3] and 1.13 eV [4]. The discrepancy can be attributed to the error associated with the limited supercell size [105,106] and the underestimation of calculated band gap of 1.26 eV relative to the experimental value of 1.42 eV. The $^4T_1$ level is predicted to be 0.42 eV above the ground level, with the associated absorption and emission at 0.44 and 0.40 eV, respectively, as listed in Table I. In experiments, a sharp emission with ZPL at 0.53 eV and a decay time on the order of millisecond [4] can be attributed to be from $^4T_1$.

Complementing the above studies, we further investigated Fe^{3+} in halides, specifically in $KMgF_3$ and $CsCdCl_3$ crystals. In the $KMgF_3$ crystal, Fe^{3+} tends to replace Mg^{2+} due to their similar ionic radii. The calculated ZPL of $^4T_1 \leftrightarrow {}^6A_1$ is 2.12 eV, which aligns well with the experimental ZPL of 1.77 eV. In the $CsCdCl_3$ perovskite, Fe^{3+} can occupy both of the two inequivalent Cd^{2+} sites, one with D_{3h} and the other with C_{3v} in point group symmetry. Our calculations show that the formation energies and defect concentrations for these substitutions are close. In Cl-rich conditions, the substituted iron primarily exists in the Fe^{3+} valence state, but transitions to Fe^{2+} in Cl-poor condition (refer to Note 2 of the Supplemental Material [47] for more details). However, the optical transitions resulting from these substitutions lead to near-infrared emissions, which do not explain the strong yellow emission observed experimentally [77,107]. Interestingly, our calculations reveal that manganese, a common contaminant, can also substitute Cd^{2+} sites and stabilize as Mn^{2+} across a wide range of chemical potentials. The calculated emission energies of the two inequivalent Mn_{oct}^{2+} are 2.13 and 1.95 eV, which are close to the experimentally observed emission peaking at 2.19 eV. This finding suggests that the observed emission can be attributed to Mn_{oct}^{2+}.

IV. CONCLUSIONS

We performed first-principles calculations on a wide variety of typical iron-doped crystals to investigate the site properties, excited states and optical properties of Fe^{3+} activators in solids, and to interpret experimental data. We determined the formation energies, ligand field strengths,

optical transition energies, and Stokes shifts of Fe^{3+} at tetrahedral, octahedral, and dodecahedral coordinated sites in a variety of hosts. Our main findings are as follows: First, we verified that Fe^{3+} can occupy tetrahedral sites in oxide insulators, producing an emission band with a peak wavelength in the range of 670 to 830 nm. A correlation was observed between the decrease in emission energy and the increase in structure distortion. Second, we found that the large ligand field strength of an octahedrally coordinated Fe^{3+} leads to a small calculated $^4T_1 \leftrightarrow ^6A_1$ transition energy. We discussed the lack of observed luminescence from octahedrally coordinated Fe^{3+} at Al^{3+} and Ga^{3+} sites in spinels and garnets, attributing the occurrence of photoluminescence in octahedral Sn^{4+}-, In^{3+}-, and Sc^{3+}-based perovskites to the much weaker ligand field resulting from larger bond lengths. Third, in hosts with a zircon structure, we attributed the red to near-infrared emissions to the dodecahedrally coordinated Fe^{3+}, comparable with the luminescence of tetrahedrally coordinated Fe^{3+}. These emissions arise from the small ligand field strength as a result of subspherical oxygen coordination distribution and small nephelauxetic effects in phosphate. Additionally, we clarified the luminescent mechanisms reported in a variety of experiments and rectified several instances of misidentification. We also calculated the $Fe^{3+} \rightarrow Fe^{2+} + h_{VBM}$ or $Fe^{4+} + e_{CBM}$ charge-transfer excitations in different crystals, providing valuable information for the identification of luminescent centers. We further examined the competition between $^4T_1$ and charge-transfer excited states, as well as the optical transitions of Fe^{3+} ion in III-V and II-VI semiconductors. In summary, this study provides a comprehensive understanding of the optical transition properties of iron impurities in a wide range of solid materials. It has implications in designing and optimizing luminescent materials.

ACKNOWLEDGMENTS

[1] D. Wickramaratne, J.-X. Shen, C. E. Dreyer, A. Alkauskas, and C. G. Van De Walle, Electrical and optical properties of iron in GaN, AlN, and InN, Phys. Rev. B **99**, 205202 (2019).

[2] A. Hoffmann, R. Heitz, and I. Broser, Fe^{3+} as near-infrared luminescence center in ZnS, Phys. Rev. B **41**, 5806 (1990).

[3] E. Malguth, A. Hoffmann, and M. R. Phillips, Fe in III-V and II-VI semiconductors, Phys. Status Solidi B **245**, 455 (2008).

[4] K. Pressel, G. Bohnert, A. Dörnen, B. Kaufmann, J. Denzel, and K. Thonke, Optical study of spin-flip transitions at Fe^{3+} in InP, Phys. Rev. B **47**, 9411 (1993).

[5] M. Godlewski and M. Skowroński, Effective deactivation of the ZnS visible photoluminescence by iron impurities, Phys. Rev. B **32**, 4007 (1985).

[6] M. Skowroński and Z. Liro, Triplet to quintet luminescence of Fe^{2+} center in ZnS, J. Lumin. **24-25**, 253 (1981).

[7] G. K. Behrh, M. Isobe, F. Massuyeau, H. Serier-Brault, E. E. Gordon, H.-J. Koo, M.-H. Whangbo, R. Gautier, and S. Jobic, Oxygen-vacancy-induced midgap states responsible for the fluorescence and the long-lasting phosphorescence of the inverse spinel Mg(Mg, Sn)O$_4$, Chem. Mater. **29**, 1069 (2017).

[8] L. Lin, Comment on "Oxygen-vacancy-induced midgap states responsible for the fluorescence and the long-lasting phosphorescence of the inverse spinel Mg(Mg, Sn)O$_4$", Chem. Mater. **32**, 7564 (2020).

[9] M. Liu, H.-Y. Kai, A. Huang, C.-K. Duan, K.-L. Wong, and P. A. Tanner, First-principles and experimental study of trace impurities and near-infrared emission in alkaline earth hexaaluminates, Chem. Mater. **35**, 2999 (2023).

[10] P. Dang, G. Zhang, W. Yang, H. Lian, G. Li, and J. Lin, Red-NIR luminescence in rare-earth and manganese ions codoped Cs$_4$CdBi$_2$Cl$_{12}$ vacancy-ordered quadruple perovskites, Chem. Mater. **35**, 1640 (2023).

[11] Y. Zhu, X. Wang, J. Qiao, M. S. Molokeev, H. C. Swart, L. Ning, and Z. Xia, Regulating Eu^{2+} multisite occupation through structural disorder toward broadband near-infrared emission, Chem. Mater. **35**, 1432 (2023).

[12] Z. Zhou, S. Zhang, Y. Le, H. Ming, Y. Li, S. Ye, M. Peng, J. Qiu, and G. Dong, Defect enrichment in near inverse spinel configuration to enhance the persistent luminescence of Fe^{3+}, Adv. Opt. Mater. **10**, 2101669 (2022).

[13] N. T. Melamed, J. Neto, T. Abritta, and F. de Souza Barros, A comparison of the luminescence of LiAl$_5$O$_8$: Fe and LiGa$_5$O$_8$: Fe–II. Fe^{3+} in octahedral sites, J. Lumin. **24-25**, 249 (1981).

[14] G. O'Connor, C. McDonagh, and T. Glynn, Luminescence from Fe^{3+} ions in octahedral sites in LiGa$_5$O$_8$, J. Lumin. **48-49**, 545 (1991).

[15] G. Pott and B. McNicol, The luminescence of Fe^{3+} and Cr^{3+} in α-gallia, J. Lumin. **6**, 225 (1973).

[16] G. Liu, S. Zhang, and Z. Xia, Multi-sites energy transfer in Fe^{3+}-doped KAl$_{11}$O$_{17}$ phosphor toward zero thermal quenching near-infrared luminescence, Opt. Lett. **48**, 1296 (2023).

[17] D. Liu, G. Li, P. Dang, Q. Zhang, Y. Wei, L. Qiu, M. S. Molokeev, H. Lian, M. Shang, and J. Lin, Highly efficient Fe^{3+}-doped A$_2$BB′O$_6$(A = Sr^{2+}, Ca^{2+}; B, B′ = In^{3+}, Sb^{5+}, Sn^{4+}) broadband near-infrared-emitting phosphors for spectroscopic analysis, Light: Sci. Appl. **11**, 112 (2022).

[18] L. Shang, Q. Chen, W. Jing, C.-G. Ma, C.-K. Duan, and J. Du, First-principles study of transition metal dopants as spin qubits, Phys. Rev. Mater. **6**, 086201 (2022).

[19] R. Heitz, P. Maxim, L. Eckey, P. Thurian, A. Hoffmann, I. Broser, K. Pressel, and B. K. Meyer, Excited states of Fe^{3+} in GaN, Phys. Rev. B **55**, 4382 (1997).

[20] E. Malguth, A. Hoffmann, and X. Xu, Internal $^5E \rightarrow ^5T_2$ transition of Fe^{2+} in GaN, Phys. Rev. B **74**, 165201 (2006).

[21] P. Alippi, F. Filippone, G. Mattioli, A. A. Bonapasta, and V. Fiorentini, Bound states of the Fe impurity in wurtzite GaN

from hybrid density-functional calculations, Phys. Rev. B **84**, 033201 (2011).

[22] U. Gerstmann, A. T. Blumenau, and H. Overhof, Transition metal defects in group-III nitrides: An *ab initio* calculation of hyperfine interactions and optical transitions, Phys. Rev. B **63**, 075204 (2001).

[23] G. M. Dalpian, J. L. F. Da Silva, and S.-H. Wei, Ferrimagnetic Fe-doped GaN: An unusual magnetic phase in dilute magnetic semiconductors, Phys. Rev. B **79**, 241201(R) (2009).

[24] X. Y. Cui, B. Delley, A. J. Freeman, and C. Stampfl, Magnetic metastability in tetrahedrally bonded magnetic III-nitride semiconductors, Phys. Rev. Lett. **97**, 016402 (2006).

[25] D. Wickramaratne, J.-X. Shen, C. E. Dreyer, M. Engel, M. Marsman, G. Kresse, S. Marcinkevičius, A. Alkauskas, and C. G. Van De Walle, Iron as a source of efficient Shockley-read-Hall recombination in GaN, Appl. Phys. Lett. **109**, 162107 (2016).

[26] A. Y. Polyakov, N. B. Smirnov, A. V. Govorkov, N. V. Pashkova, A. A. Shlensky, S. J. Pearton, M. E. Overberg, C. R. Abernathy, J. M. Zavada, and R. G. Wilson, Electrical and optical properties of Cr and Fe implanted n-GaN, J. Appl. Phys. **93**, 5388 (2003).

[27] G. Kresse and J. Hafner, *Ab initio* molecular dynamics for liquid metals m, Phys. Rev. B **47**, 558 (1993).

[28] G. Kresse and J. Hafner, *Ab initio* molecular-dynamics simulation of the liquid-metal–amorphous-semiconductor transition in germanium, Phys. Rev. B **49**, 14251 (1994).

[29] J. P. Perdew, K. Burke, and M. Ernzerhof, Generalized gradient approximation made simple, Phys. Rev. Lett. **77**, 3865 (1996).

[30] P. E. Blöchl, Projector augmented-wave method, Phys. Rev. B **50**, 17953 (1994).

[31] B. J. Wood, R. J. Kirkpatrick, and B. Montez, Order-disorder phenomena in $MgAl_2O_4$ spinel, Am. Mineral. **71**, 999 (1986).

[32] M. Gaudon, A. Apheceixborde, M. Ménétrier, A. L. Nestour, and A. Demourgues, Synthesis temperature effect on the structural features and optical absorption of $Zn_{1-x}Co_xAl_2O_4$ oxides, Inorg. Chem. **48**, 9085 (2009).

[33] R. Millard, R. Peterson, and I. Swainson, Synthetic $MgGa_2O_4$-Mg_2GeO_4 spinel solid solution and β-$Mg_3Ga_2GeO_8$: Chemistry, crystal structures, cation ordering, and comparison to Mg_2GeO_4 olivine, Phys. Chem. Miner. **27**, 179 (2000).

[34] M. M. Can, G. Hassnain Jaffari, S. Aksoy, S. I. Shah, and T. Fırat, Synthesis and characterization of $ZnGa_2O_4$ particles prepared by solid state reaction, J. Alloys Compd. **549**, 303 (2013).

[35] J. Sappl, F. Jung, and C. Hoch, Facile one-step syntheses of several complex ionic lithium gallates from liga as intermetallic precursors, Chem. Mater. **32**, 866 (2020).

[36] S. J. Kim, Z. C. Chen, and A. V. Virkar, Phase transformation kinetics in the doped system $LiAl_5O_8$-$LiFe_5O_8$, J. Am. Ceram. Soc. **71**, C428 (1988).

[37] D. Rodic, M. Mitric, R. Tellgren, and H. Rundlof, The cation distribution and magnetic structure of $Y_3Fe_{5-x}Al_xO_{12}$, J. Magn. Magn. Mater. **232**, 1 (2001).

[38] A. Verma, N. Malhan, and A. K. Ganguli, Preparation, structure and characterization of nanocrystalline-Nd:$Y_3Ga_5O_{12}$, Mater. Lett. **81**, 242 (2012).

[39] X. Liu, L. Zhu, L. Wang, C. Yu, and J. Lin, Synthesis and luminescent properties of $Lu_3Ga_5O_{12}$:RE^{3+} (RE = Eu, Tb, and Pr) nanocrystalline phosphors via sol-gel process, J. Electrochem. Soc. **155**, P21 (2008).

[40] A. Faik, D. Orobengoa, E. Iturbe-Zabalo, and J. Igartua, A study of the crystal structures and the phase transitions of the ordered double perovskites Sr_2ScSbO_6 and Ca_2ScSbO_6, J. Solid State Chem. **192**, 273 (2012).

[41] S. E. Rasmussen, J.-E. Jørgensen, and B. Lundtoft, Refinement of the structure of $ScPO_4$ by powder diffr. by three Rietveld programs, Powder Diffr. **8**, 164 (1993).

[42] Y. Ni, J. M. Hughes, and A. N. Mariano, Crystal chemistry of the monazite and xenotime structures, Am. Mineral. **80**, 21 (1995).

[43] W. Milligan, D. Mullica, G. Beall, and L. Boatner, Structural investigations of YPO_4, $ScPO_4$, and $LuPO_4$, Inorg. Chim. Acta **60**, 39 (1982).

[44] I. V. Bodnar, Growth and properties of $CuAlS_{2x}Se_{2(1-x)}$ single crystals, Inorg. Mater. **38**, 647 (2002).

[45] R. C. DeVries and R. Roy, Fluoride models for oxide systems of dielectric interest. the systems KF-MgF_2 and AgF-ZnF_2, J. Am. Chem. Soc. **75**, 2479 (1953).

[46] Y. Huang, Y. Pan, S. Guo, C. Peng, H. Lian, and J. Lin, Large spectral shift of Mn^{2+} emission due to the shrinkage of the crystalline host lattice of the hexagonal $CsCdCl_3$ crystals and phase transition, Inorg. Chem. **61**, 8356 (2022).

[47] See Supplemental Material at http://link.aps.org/supplemental/10.1103/PhysRevB.109.165124 for (note 1) the discussion on computational settings and convergence tests; (note 2) the influence of chemical potentials on defect formation energies; (Fig. S1) the projected density of states and schematic nominal electronic occupancy of Fe^{3+} for ground and excited states; (Fig. S2) partial charge density distributions of KS orbitals for excited states; (Figs. S3– S9) the influence of chemical potentials on defect formation energies; (Fig. S10) the pressure dependence of $^4T_1 \rightarrow {}^6A_1$ emission energy of Fe^{3+} in the β-$LiGaO_2$ host; (Fig. S11) changes of bond length versus mismatch in ion radius; (Fig. S12) calculated vs experimental $^4T_1 \rightarrow {}^6A_1$ emission energy, which includes Refs. [31–46,48–51].

[48] L. Wang, T. Maxisch, and G. Ceder, Oxidation energies of transition metal oxides within the GGA + U framework, Phys. Rev. B **73**, 195107 (2006).

[49] A. Jain, G. Hautier, S. P. Ong, C. J. Moore, C. C. Fischer, K. A. Persson, and G. Ceder, Formation enthalpies by mixing GGA and GGA + *U* calculations, Phys. Rev. B **84**, 045115 (2011).

[50] S. L. Dudarev, G. A. Botton, S. Y. Savrasov, C. J. Humphreys, and A. P. Sutton, Electron-energy-loss spectra and the structural stability of nickel oxide: An LSDA+*U* study, Phys. Rev. B **57**, 1505 (1998).

[51] T. O. Wehling, A. I. Lichtenstein, and M. I. Katsnelson, Transition-metal adatoms on graphene: Influence of local Coulomb interactions on chemical bonding and magnetic moments, Phys. Rev. B **84**, 235110 (2011).

[52] C. Freysoldt, B. Grabowski, T. Hickel, J. Neugebauer, G. Kresse, A. Janotti, and C. G. Van de Walle, First-principles calculations for point defects in solids, Rev. Mod. Phys. **86**, 253 (2014).

[53] C. G. Van de Walle and J. Neugebauer, First-principles calculations for defects and impurities: Applications to III-nitrides, J. Appl. Phys. **95**, 3851 (2004).

[54] Q. Chen, M. Liu, C.-G. Ma, and C.-K. Duan, Mechanistic insights for regulating the site occupancy, valence states and optical transitions of Mn ions in yttrium-aluminum garnets via codoping, Phys. Chem. Chem. Phys. **25**, 18808 (2023).

[55] Q. Chen, L. Shang, C.-G. Ma, and C.-K. Duan, Angular Jahn-Teller effect and photoluminescence of the tetrahedral coordinated Mn^{2+} activators in solids—A first-principles study, Inorg. Chem. **61**, 13471 (2022).

[56] S. Sugano, *Multiplets of Transition-Metal Ions in Crystals* (Academic Press, New York, 2012).

[57] J. P. Allen and G. W. Watson, Occupation matrix control of d- and f-electron localisations using DFT+U, Phys. Chem. Chem. Phys. **16**, 21016 (2014).

[58] W. Jing, M. Liu, X. Wei, C.-G. Ma, M. Yin, and C.-K. Duan, Defect levels of $3d^n$ transition-metal series in wide-gap oxide and fluoride insulators: A first-principles study, Phys. Rev. B **106**, 075110 (2022).

[59] L. Pan, Y. Wang, L. Yin, L. Zhang, Y. Li, P. Townsend, and D. Poelman, Structural and optical properties of iron ions doped near-infrared persistent spinel-type phosphors, J. Lumin. **258**, 119822 (2023).

[60] M. Li, Y. Jin, L. Yuan, B. Wang, H. Wu, Y. Hu, and F. Wang, Near-infrared long afterglow in Fe^{3+}-activated Mg_2SnO_4 for self-sustainable night vision, ACS Appl. Mater. Interfaces **15**, 13186 (2023).

[61] K. Kniec, W. Piotrowski, K. Ledwa, L. D. Carlos, and L. Marciniak, Spectral and thermometric properties altering through crystal field strength modification and host material composition in luminescence thermometers based on Fe^{3+} doped AB_2O_4 type nanocrystals (A = Mg, Ca; B = Al, Ga), J. Mater. Chem. C **9**, 517 (2021).

[62] L. P. Sosman, A. Dias Tavares Jr., P. S. Silva, and T. Abritta, Optical spectroscopy of $MgGa_2O_4$: Fe^{3+}, Phys. Status Solidi A **176**, 1085 (1999).

[63] L. Xiang, X. Zhou, Y. Wang, L. Li, S. Jiang, G. Xiang, C. Jing, J. Li, and L. Yao, Environmentally-friendly and low-cost Fe^{3+}-doped broadband NIR light-emitting phosphors, J. Lumin. **252**, 119293 (2022).

[64] J. Neto, T. Abritta, F. de S. Barros, and N. Melamed, A comparative study of the optical properties of Fe^{3+} in ordered $LiGa_5O_8$ and $LiAl_5O_8$, J. Lumin. **22**, 109 (1981).

[65] C. McShera, P. Colleran, T. Glynn, G. Imbusch, and J. Remeika, Luminescence study of $LiGa_{5-x}Fe_xO_8$, J. Lumin. **28**, 41 (1983).

[66] T. Abritta, F. de Souza Barros, and N. Melamed, Luminescence of Fe^{3+} in single crystals of $LiAl_5O_8$, J. Lumin. **33**, 141 (1985).

[67] S. Panda, P. Vinodkumar, M. Sahoo, U. Madhusoodanan, and B. Panigrahi, Probing the site occupancy of dopants in deep red-NIR emitting $LiAl_5O_8$: Eu^{3+}, Cr^{3+}, and Fe^{3+} nano phosphors using photoluminescence and x-ray absorption spectroscopy, J. Alloys Compd. **857**, 157615 (2021).

[68] N. Melamed, P. Viccaro, J. Artman, and F. De S. Barros, The fluorescence of Fe^{3+} in ordered and disordered phases of $LiAl_5O_8$, J. Lumin. **1-2**, 348 (1970).

[69] X. Zhou, X. Luo, B. Wu, S. Jiang, L. Li, X. Luo, and Y. Pang, The broad emission at 785nm in YAG: Ce^{3+}, Cr^{3+} phosphor, Spectrochim. Acta, Part A **190**, 76 (2018).

[70] K. Kniec, K. Ledwa, K. Maciejewska, and L. Marciniak, Intentional modification of the optical spectral response and relative sensitivity of luminescent thermometers based on Fe^{3+}, Cr^{3+}, Nd^{3+} co-doped garnet nanocrystals by crystal field strength optimization, Mater. Chem. Front. **4**, 1697 (2020).

[71] Z. Kang-Wei, X. Jun-Kai, N. You-Ming, Z. Sang-Bo, and W. Ping-Feng, Crystal-field theory and the s-state splitting of Fe^{3+} in yttrium gallium garnet, Phys. Rev. B **44**, 7499 (1991).

[72] E. Oomen, K. V. D. Vlist, W. Smit, and G. Blasse, Luminescence of iron(III): In zircon-structured phosphates MPO_4 (M = Sc, Lu, Y), Chem. Phys. Lett. **129**, 9 (1986).

[73] R. Müller, M. Mangold, S. Bauer, F. Huber, U. Herr, and K. Thonke, Zeeman spectroscopy of the internal transition $^4T_1$ to $^6A_1$ of Fe^{3+} ions in ZnO, J. Appl. Phys. **132**, 065702 (2022).

[74] R. Heitz, A. Hoffmann, and I. Broser, Fe^{3+} center in ZnO, Phys. Rev. B **45**, 8977 (1992).

[75] K. Sato and T. Teranishi, Infrared luminescence of Fe^{3+} in $CuGaS_2$ and $CuAlS_2$, J. Phys. Soc. Jpn. **37**, 415 (1974).

[76] A. Poirier and D. Walsh, Photoluminescence of iron-doped $KMgF_3$, J. Phys. C: Solid State Phys. **16**, 2619 (1983).

[77] S. Ge, Q. Wei, W. Jia, Y. Liang, C. Peng, Y. Tian, and B. Zou, Strong yellow emission of polaronic magnetic exciton in Fe^{3+}-doped $CsCdCl_3$ perovskites, Appl. Phys. Lett. **118**, 152102 (2021).

[78] R. Kobayashi, H. Tamura, Y. Kamada, M. Kakihana, and Y. Matsushima, A new host compound of aluminum lithium fluoride oxide for deep red phosphors based on Mn^{4+}, Fe^{3+}, Cr^{3+}, ECS Trans. **88**, 225 (2018).

[79] S. Kück and S. Hartung, Comparative study of the spectroscopic properties of Cr^{4+}-doped $LiAlO_2$ and $LiGaO_2$, Chem. Phys. **240**, 387 (1999).

[80] X. Feng, L. Lin, R. Duan, J. Qiu, and S. Zhou, Transition metal ion activated near-infrared luminescent materials, Prog. Mater. Sci. **129**, 100973 (2022).

[81] F. Liu, Y. Liang, Y. Chen, and Z. Pan, Divalent nickel-activated gallate-based persistent phosphors in the short-wave infrared, Adv. Opt. Mater. **4**, 562 (2016).

[82] B. Wu, J. Ruan, J. Ren, D. Chen, C. Zhu, S. Zhou, and J. Qiu, Enhanced broadband near-infrared luminescence in transparent silicate glass ceramics containing Yb^{3+} ions and Ni^{2+}-doped $LiGa_5O_8$ nanocrystals, Appl. Phys. Lett. **92**, 041110 (2008).

[83] G. K. Kosgei, P. U. A. I. Fernando, J. S. Forrester, E. M. Alberts, B. M. Fernando, D. L. Henderson, and C. A. Weiss Jr, Exploring the luminescence of tin-incorporated nickel-sensitized lithium gallate short-wave-infrared phosphors, J. Am. Ceram. Soc. **106**, 6342 (2023).

[84] J. Donegan, F. Bergin, T. Glynn, G. Imbusch, and J. Remeika, The optical spectroscopy of $LiGa_5O_8$: Ni^{2+}, J. Lumin. **35**, 57 (1986).

[85] Z. Zhou, X. Yi, P. Xiong, X. Xu, Z. Ma, and M. Peng, Cr^{3+}-free near-infrared persistent luminescence material $LiGaO_2$: Fe^{3+}: Optical properties, afterglow mechanism and potential bioimaging, J. Mater. Chem. C **8**, 14100 (2020).

[86] A. K. Somakumar, L.-I. Bulyk, V. Tsiumra, J. Barzowska, P. Xiong, A. Lysak, Y. Zhydachevskyy, and A. Suchocki, Inorg. Chem. **62**, 12434 (2023).

[87] G. B. Scott, D. E. Lacklison, and J. L. Page, Absorption spectra of $Y_3Fe_5O_{12}$ (YIG) and $Y_3Ga_5O_{12}$: Fe^{3+}, Phys. Rev. B **10**, 971 (1974).

[88] A. Anedda, C. M. Carbonaro, D. Chiriu, R. Corpino, M. Marceddu, and P. C. Ricci, Electron-phonon coupling in iron-doped yttrium aluminum garnet, Phys. Rev. B **74**, 245108 (2006).

[89] P. C. Ricci, A. Casu, and A. Anedda, Effect of the electron-phonon interaction on the luminescence properties of iron ions in YAG crystal, J. Phys. Chem. A **113**, 13901 (2009).

[90] Y. Yang, L. Shen, J. Zhang, S. Zhao, Q. Pang, X. Zhang, P. Chen, and L. Zhou, Tetracoordinate Fe^{3+} activated Li_2ZnAO_4(A = Si, Ge) near-infrared luminescent phosphors, Inorg. Chem. **62**, 12862 (2023).

[91] Y.-P. Wang, H.-S. Zhang, L.-T. Lin, S.-F. Zhou, Y. Yao, X.-B. Yang, and Y.-J. Zhao, Role of intrinsic defects on the persistent luminescence of pristine and Mn doped $ZnGa_2O_4$, J. Appl. Phys. **125**, 095701 (2019).

[92] Q. Chen, L. Shang, H. Xu, C. Ma, and C.-K. Duan, Multiple-valence and visible to near-infrared photoluminescence of manganese in $ZnGa_2O_4$: A first-principles study, J. Phys. Chem. C **125**, 21780 (2021).

[93] S. Kück, S. Hartung, S. Hurling, K. Petermann, and G. Huber, Optical transitions in Mn^{3+}-doped garnets, Phys. Rev. B **57**, 2203 (1998).

[94] Q. Chen, L. Shang, H. Xu, C. Ma, P. A. Tanner, and C.-K. Duan, Rationalizing the structural changes and spectra of manganese and their temperature dependence in a series of garnets with first-principles calculations, Phys. Rev. B **105**, 035158 (2022).

[95] Q. Chen, M. Liu, L. Shang, and C.-K. Duan, Elucidating the multisite and multivalence nature of Mn ions in solids and predicting their optical transition properties: A case study on a series of garnet hosts, Inorg. Chem. **61**, 18690 (2022).

[96] X. Zhang, D. Chen, X. Chen, C. Zhou, P. Chen, Q. Pang, and L. Zhou, Broadband near-infrared luminescence from Fe^{3+}-activated $NaScSi_2O_6$ phosphors for luminescence ther-

mometry and night-vision applications, Dalton Trans. **51**, 14243 (2022).

[97] D. L. Dexter, C. C. Klick, and G. A. Russell, Criterion for the occurrence of luminescence, Phys. Rev. **100**, 603 (1955).

[98] M. C. Marco de Lucas, M. Moreno, F. Rodriguez, and P. G. Baranov, Luminescence from samples: Substitutional ions are 'silent', J. Phys.: Condens. Matter **8**, 2457 (1996).

[99] R. H. Awater and P. Dorenbos, The $Bi^{3+}6s$ and $6p$ electron binding energies in relation to the chemical environment of inorganic compounds, J. Lumin. **184**, 221 (2017).

[100] O. Madelung, *Semiconductors–Basic Data* (Springer Science & Business Media, 2012).

[101] H. Raebiger, S. Bae, C. Echeverría-Arrondo, and A. Ayuela, Control of hole localization in magnetic semiconductors by axial strain, Phys. Rev. Mater. **2**, 024402 (2018).

[102] J. Baur, K. Maier, M. Kunzer, U. Kaufmann, J. Schneider, H. Amano, I. Akasaki, T. Detchprohm, and K. Hiramatsu, Infrared luminescence of residual iron deep level acceptors in gallium nitride (GaN) epitaxial layers, Appl. Phys. Lett. **64**, 857 (1994).

[103] J. Dieleman, J. W. De Jong, and T. Meijer, Acceptor action of alkali metals in II–VI compounds as detected by electron spin resonance techniques, J. Chem. Phys. **45**, 3178 (1966).

[104] H. Zimmermann, R. Boyn, and N. Nagel, Photoinduced absorption spectra of ZnS:Fe crystals, Phys. Status Solidi B **117**, 229 (1983).

[105] J. Strand, S. K. Chulkov, M. B. Watkins, and A. L. Shluger, First principles calculations of optical properties for oxygen vacancies in binary metal oxides, J. Chem. Phys. **150**, 044702 (2019).

[106] S. R. Kavanagh, C. N. Savory, S. M. Liga, G. Konstantatos, A. Walsh, and D. O. Scanlon, Frenkel excitons in vacancy-ordered titanium halide perovskites Cs_2TiX_6, J. Phys. Chem. Lett. **13**, 10965 (2022).

[107] P. J. S. Rana, T. Swetha, H. Mandal, A. Saeki, P. R. Bangal, and S. P. Singh, Energy transfer dynamics of highly stable Fe^{3+} doped $CsPbCl_3$ perovskite nanocrystals with dual-color emission, J. Phys. Chem. C **123**, 17026 (2019).